CONTENTS Page

Research papers

Soumia Hamza, Zakaria Boumerzoug, Elhadj Raouache, Fabienne Delaunois
Simulated heat affected zone in welded stainless steel 304L **142**

Le Thai Hung, Vu Thi Dinh, Doan Thi Phuong, Le Trung Kien
Effect of springback in DP980 advanced high strength steel on product precision in bending process **150**

Duong Nam Nguyen, Duong-Nguyen Nguyen, Mai Khanh Pham
Influence of rare-earth on the microstructure and mechanical properties of high manganese steel under impact load **158**

Jozef Petrík, Peter Blaško, Andrea Vasilňaková, Peter Demeter, Peter Futaš
Indentation size effect of heat treated aluminum alloy **166**

Bui Duc Long, Nguyen Van Khanh, Duong Ngoc Binh, Le Hong Thang, Le Thi Bang, Suhana Binti Mohd Said
Synthesis of Cu_2ZnSnS_4 by mechanical alloying method for thermoelectric application **174**

Matías Humberto Sosa Lissarrague, Alejandro Sepulveda Buitrago, Alberto Carlos Picasso
Study of $M_{23}C_6$ precipitation in A 45Ni-35Cr-Nb alloy **180**

Yen Ngoc Nguyen, Tu Anh Dao, Hai Minh Le, Khanh Quoc Dang, Makoto Nanko
Fabrication of transparent $MgAl_2O_4$ spinel ceramics by pecs processing of combustion - sythesized nanopowders **186**

Lilik Dwi Setyana, Muslim Mahardika, Sutiyoko, Suyitno
Influence of gate shape and direction during centrifugal casting on artificial lumbar disc model of Cp-Ti **193**

DOI 10.12776/ams.v25i3.1319 p-ISSN 1335-1532
e-ISSN 1338-1156

SIMULATED HEAT AFFECTED ZONE IN WELDED STAINLESS STEEL 304L

*Soumia Hamza[1)], Zakaria Boumerzoug[1) *], Elhadj Raouache[2)], Fabienne Delaunois[3)]*
[1)] Department of Mechanical Engineering, LMSM, University of Biskra, Biskra, Algeria
[2)] Department of Civil Engineering, University of B.B.A, Algeria
[3)] Faculté Polytechnique de Mons 56, rue de l'Epargne, B-7000 Mons, Belgique

Received: 30.05.2019
Accepted: 16.09.2019

[*]Corresponding author: e-mail :zboumerzoug@yahoo.fr, Tel.:+213775759694, Department of Mechanical Engineering, LMSM, University of Biskra, B.P. 145, Biskra, Algeria

Abstract
This work is a contribution study of the heat-affected zone in the real welded joint of stainless steel 304L. This zone was compared to the heat-affected zone obtained by using a thermal cycle simulation of welding. This experimental technique is based on thermal cycle simulation of welding by rapid heating and cooling treatments of the base metal in a specific simulation equipment. The samples were analyzed by scanning electron microscopy equipped with energy dispersive X-ray, and microhardness measurements. Microstructures and mechanical properties of the simulated heat affected zone were also determined. Thermal cycle simulation technique has revealed more details on the microstructure and the mechanical behavior of the heat-affected zone.

Keywords: stainless steel, thermal cycle simulation, welding, microstructures, microhardness

1 Introduction

Austenitic stainless steels are the most common and familiar types of stainless steel. They are most extremely formable and weldable [1]. Among the many 300 series austenitic stainless steel grades, AISI 304L stainless steels are extensively used in industries due to their superior low temperature toughness and high corrosion resistance [2]. Additionally, it is among the cheapest grades of stainless steels, making it the favourite choice of industry. American Iron and Steel Institute (AISI) type 304 is the formation of 300 series austenitic stainless steels is by far the oldest, largest and most important group in the stainless steel range. The L grades represent low-carbon variants with nominal carbon level of 0.03 % depending on the specification to which is manufactured, which are used for general stainless steel fabrication, elevated temperature applications and resistance to pitting corrosion [3].

It is known that the heat generated during welding induces an important temperature gradient in and around the welded area. The region outside the welded joint that is thermally affected by the welding treatment is known as the heat-affected zone (HAZ) [4]. Its property and microstructure are affected by the thermal cycle. The mechanical properties of the welded metal and the HAZ are closely related to their microstructures, which are dependent on the chemical composition of the material and the thermal history (cycles) due to the welding processes [5, 6]. The welded joints under exploitation conditions can be affected by the chemical heterogeneity or mechanical properties of base material, heat affected zone and weld metal. It has been concluded that by improving the microstructure of the HAZ, the properties of the welded joint can be improved [7]. Excessive heat input could result in a wide HAZ with low impact strength [8]. As reported

DOI 10.12776/ams.v25i3.1290 p-ISSN 1335-1532
e-ISSN 1338-1156

by Gu et al. [9], the degradation in strength and toughness of welded joint, is always happens in HAZ.

For this reason, weld thermal cycle simulation can be used for optimizing the welding technology since it enables some mechanical testing for properties that cannot be made on real welded joints because of small width of HAZ. Weld thermal cycle simulation facilitates gaining of results needed for optimization of high-alloy steel welding parameters, which can be further used for real-conditioned welding [10]. This technique consisted of rapid heating and cooling treatments of the base metal in specific simulation equipment. The HAZ can be simulated by heating the base metal at different temperatures, which correspond to the temperature at HAZ of the real welded joint. This technique has been used in our previous works [8, 11]. We studied the heat-affected zone by thermal cycle simulation of welded INC 738 LC alloy [11] and low carbon steel [6]. We found a similarity between the microstructure obtained by thermal cycle simulation of welding and the microstructure of the HAZ of the real welded joint.

We notice that the previous work on welding of 304L stainless steel were focused on microstructure and corrosion behavior of welded material [12-14] and there is not a specific investigation on heat affected zone of welded 304L stainless steel. The objective of this present investigation is to study the microstructures of the HAZ of 304L stainless steel by a thermal cycle simulation.

2 Experimental materials and methods

The base metal (BM) is AISI 304L Austenitic stainless steel which is used for transport gas pipeline applications, generally welded for pipeline construction. The chemical composition of 304L steel is presented in **Table 1**.

Table 1 Chemical composition of AISI 304L austenitic stainless steel (wt %)

Fe	C	Mn	Si	P	S	Ni	Cr
Balance	0.026	1 .07	0.40	0.038	0.001	8.11	18.50

To obtain real welded joint, V-shaped butt welds were prepared using two consecutive passes with gas tungsten arc welding (GTAW) method and ER-308L filler was used as electrode. The chemical composition of the electrode is presented in **Table 2**. In addition, argon gas was used during welding to avoid a penetration into weld region of some undesirable elements (N_2, O_2, H_2).

Table 2 Chemical composition of the electrode (Wt.%).

Fe	C	Mn	Si	P	S	Ni	Cr
Balance	0.026	1 .07	0.40	0.038	0.001	8.11	18.50

For thermal cycle simulation study, specimens 10 mm thick 10 x 57 mm^2 of AISI 304L Austenitic stainless steel, were heat treated for the simulator tests TCS 1405 (**Fig. 1**). Simulation studies of thermal cycles consisted of resistive heating of samples. Based on phase diagram of Fe-Cr, thermal cycles were simulated at the following temperatures: 600°C, 700°C, 800°C, 900°C, 1100°C, and 1200°C (**Fig. 2**).

DOI 10.12776/ams.v25i3.1290 p-ISSN 1335-1532
e-ISSN 1338-1156

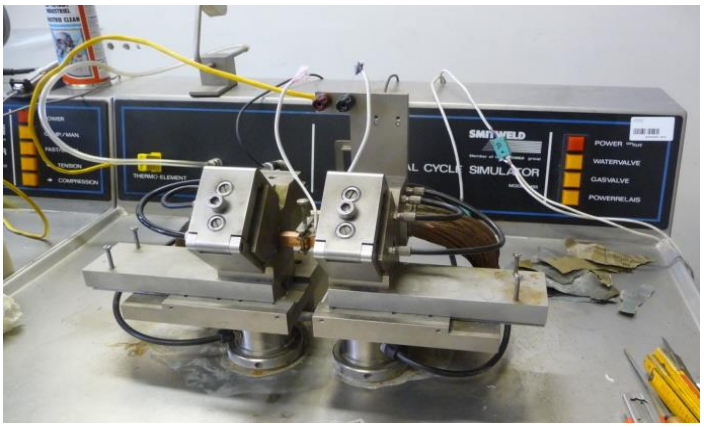

Fig. 1 Smitweld thermal cycle simulator in application

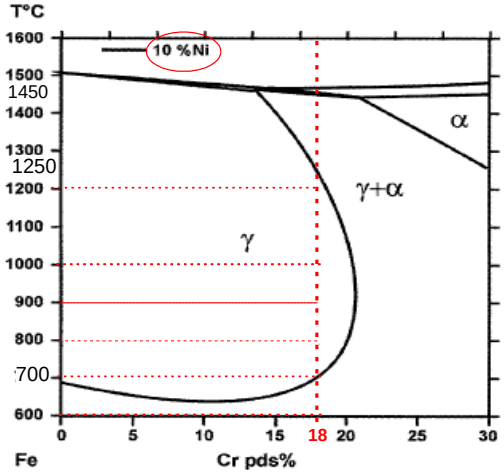

(a) **(b)**

Fig. 2 (a): Equilibrium diagram of Fe-Cr [5] and (b) heated samples by thermal cycle simulator

The specimens for metallographic examination were polished using different grades of emery papers. Final polishing was done using the diamond compound (0.5 μm particle size) in the disc-polishing machine. Samples were etched with V2A reagent to reveal the microstructure. The etched samples were observed by Scanning Electron Microscopy (SEM) Bruker, which is equipped with en energy dispersive X-ray (EDS) detector for chemical composition microanalysis. Vickers's microhardness testing machine was employed for measuring the hardness of the specimens with 0.1 kg load**.**

3 Results and discussion

3.1 EDS analysis and microstructure of the base metal

The EDS spctrum of the AISI 304L austenitic stainless steel is presented in **Fig. 3**. The main alloying elements (Cr, Ni, Mn, Si) were detected.

DOI 10.12776/ams.v25i3.1290 p-ISSN 1335-1532
e-ISSN 1338-1156

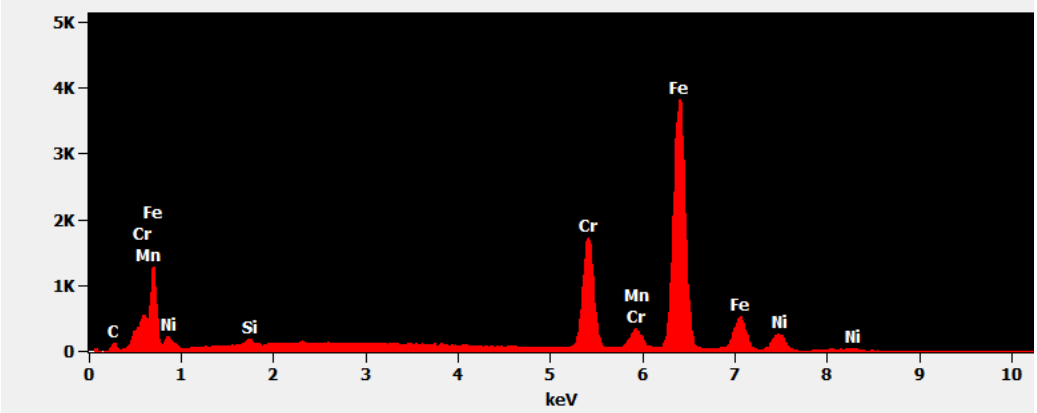

Fig. 3 EDS spctrum of AISI 304L austenitic stainless steel

The microstructure of the AISI 304L austenitic stainless steel is homogeneous and it is mainly composed of austenite phase (**Fig. 4**).

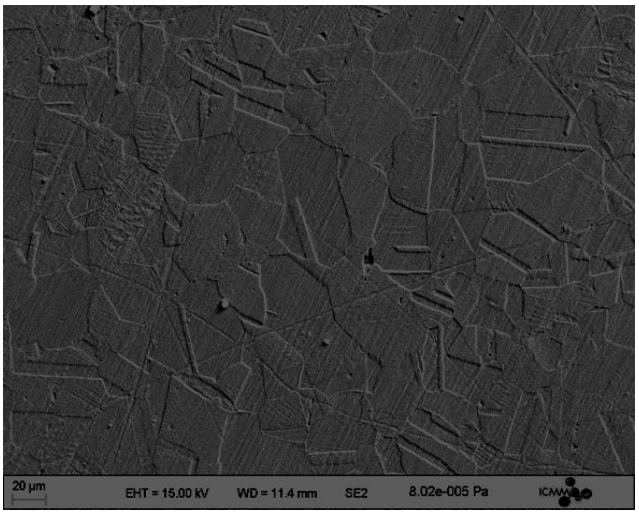

Fig. 4 Microstructure of the stainless steel 304L

3.2 Microstructure and hardness Vickers of the real welded joint

Generally, the metallurgy of the welded joint can be categorised into two major regions, the fusion zone (FZ) and the heat-affected zone (HAZ). **Fig. 5** presents the microstructure of the welded joint of the stainless steel 304L with the average hardness value of each zone. In this case, it is easy to distinguish the FZ to the rest of the zones (HAZ and BM). FZ is delimited by yellow discontinuous line. However, it is not easy to make a difference between the HAZ and BM. In addition, there is a slight difference between the hardness values between the three zones (BM, HAZ and FZ). For this reason, the investigation of HAZ by thermal cycle simulation welding is necessary.

DOI 10.12776/ams.v25i3.1290 p-ISSN 1335-1532
e-ISSN 1338-1156

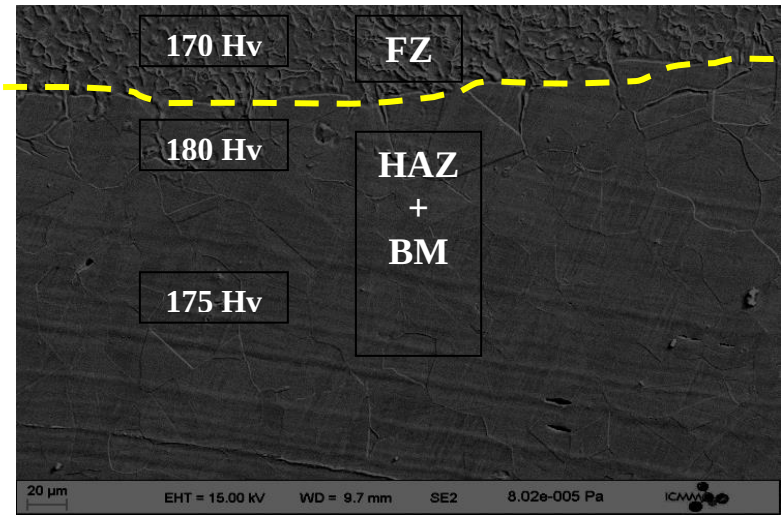

Fig. 5 Microstructure of the welded joint of stainless steel 304L

3.3 Microstructures and hardness after thermal cycles

Fig. 6 shows the microstructures of stainless steel 304L obtained after different thermal cycles (600, 700, 800, 900, 1100, and 1200 °C) with the corresponding hardness value respectively (297.85, 227.87, 225.35, 225.25, 163.500, and 162.50 Hv). The main observed transformation was the development of the grain growth reaction during the thermal cycle at 1200 °C. At this temperature, the mobility of the grain boundaries is higher as indicated by an arrow, which corresponds to the regeneration of new grains. It has been reported that austenitic steels may undergo microstructural changes in the course of the welding process or when they are exposed to elevated temperature for a shorter or longer period of time [15]. The thermal cycle at 800°C and 900 °C leads to the carbide formation as indicated by square in figure 6. The main carbides observed in 304L steel were Mn_5C_2, Mn_7C_3 and $Mn_{23}C_6$ [16]. These hardened compound phases contribute to the increase of the hardness in HAZ.

However, with the increase of temperature more than 900 °C, the hardness HV decreases. This decrease is due to grain growth and dissolution of the carbides. It could be also attributed to a lower stress level and to change in microstructure as it has been found by Kozuh et al. [17, 18]. These authors studied the mechanical properties and microstructure of austenitic stainless steel after welding and post-weld heat treatment. In addition to this work, it has been found also that the coarse grain formation in the HAZ occurring by recrystallization and grain growth in fully austenitic metals increases susceptibility to liquation cracking, while ferrite forming composition are not susceptible [18].

Based on the above results we can deduce that the HAZ is not a homogeneous structure but it can be divided in successive subzones. The microstructure and the hardness change from the base metal to the fusion zone, i.e., the microstructure of the nearest subzone to the FZ has the lowest hardness and the highest grains size; however the nearest subzone to the BM has the highest hardness and the lowest grains size. Jelani et al. [19] concluded that the sensitivity of the mechanical properties of 304L stainless steel to temperature, i.e., the material becomes softer and more ductile with the increase of the temperature up to 900 °C. For this reason, the nearest subzone to the FZ has the lowest hardness. These hardness values are more precise than the hardness values measured on the real welded joint.

DOI 10.12776/ams.v25i3.1290 p-ISSN 1335-1532
e-ISSN 1338-1156

(a)

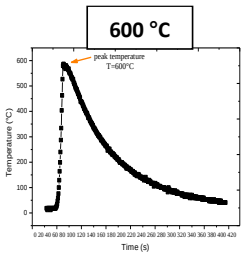

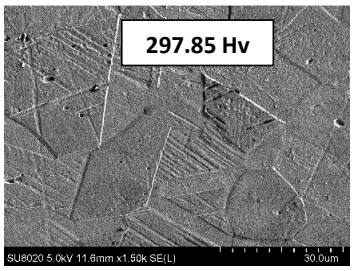

(b)

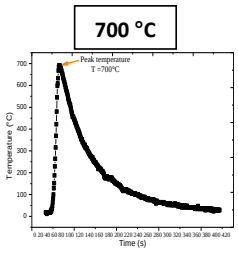

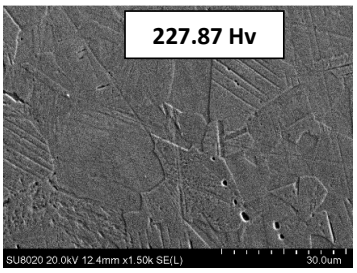

(c)

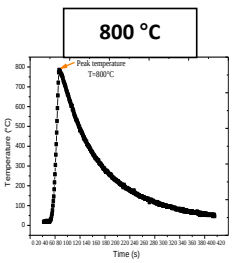

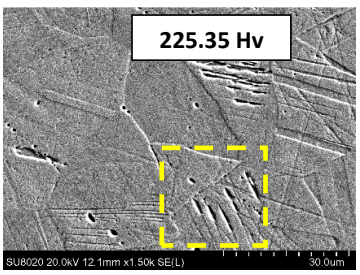

.

(d)

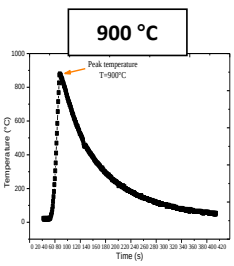

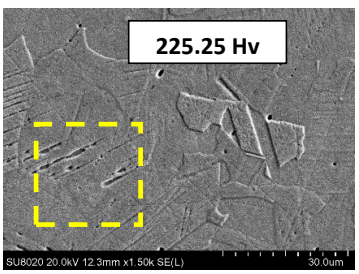

(e)

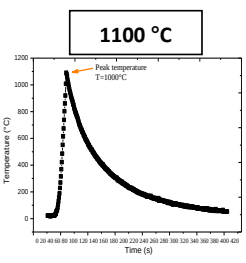

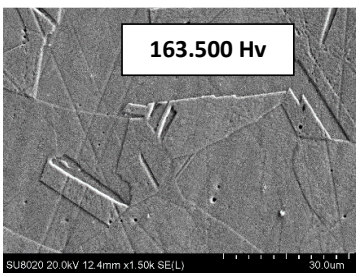

DOI 10.12776/ams.v25i3.1290
p-ISSN 1335-1532
e-ISSN 1338-1156

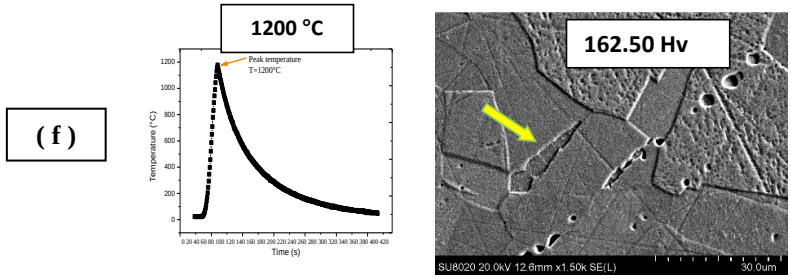

Fig. 6 Microstructures of 304L after simulation welding process and their plotted temperature-time during the welding thermal cycle (a-f)

4 Conclusion

In summary, the simulated HAZ of the welded stainless steel 304L has been investigated by the thermal cycle simulation technique and compared to the HAZ obtained from the real welded joint. The microstructural observation of the HAZ in real welded joint did not reveal more details. However, the investigation of the simulated HAZ by the thermal cycle simulation technique has given more information. The HAZ is not a homogeneous structure but it is formed with different subzones. The thermal cycle at 800 and 900 °C leads to the carbide formation. By increasing the temperature by simulation technique, the HAZ becomes softer which corresponds to the nearest subzone to the FZ. This softening phenomenon is due to the grain growth and the dissolution of carbides.

References

[1] M. McGuire, Stainless steel for design engineers, ASM International, Materials Park, Ohio, 2008
[2] WF. Smith, Structure and properties of engineering alloys, 2nd ed. New York: McGraw-Hill; 1993
[3] P. S. Korinko, S. H. Malene, Consideration for the weldability of types 304L and 316L stainless steels, Department of energy, U.S. 2001
[4] A. Mostafa, S. Bordbar,: Materials Letters, 98, 2013, 178–181, http://dx.doi.org/10.1016/j.matlet.2013.04.035
[5] Y. Chen, Y. Y. Wang, J. Gianetto: Proceedings of the Eighteenth International Offshore and Polar Engineering Conference, Vancouver, BC, Canada, July 6–11, 2008
[6] Z. Boumerzoug E. Raouache Elhadj, F. Delaunois: Materials Science and Engineering A 530 ,2011, 191–195, http://dx.doi.org/10.1016/j.msea.2011.09.073
[7] K. Digheche, Z. Boumerzoug, M. Diafi : Acta metallurgica Slovaca, Vol. 23, No. 1, 2017, 72-78, http://dx.doi.org/10.12776/ams.v23i1.879
[8] V. Gunaraj, N. Murugan: Welding research, 81, 2002, p. 94-98
[9] Y. H. Guo, L. Lin, D. Zhang, L. Liu, M. K. Lei: Metals, Vol. 8, 2018, No. 773, p.1-14 http://dx.doi.org/10.3390/met8100773
[10] M. Dunđer, I. Samardžić, T. Vuherer: Metalurgija, Vol. 54, 2015, No. 3, p. 539-542
[11] Z. Boumerzoug et S. Cherif : Key Engineering Materials, Vol. 735, 2017, p. 75-79 http://dx.doi.org/10.4028/www.scientific.net/KEM.735.75
[12] G. R. Mirshekari, E. Tavakoli, M. Atapour, B. Sadeghian: Materials and Design, Vol. 55, 2014, p. 905–911, http://dx.doi.org/10.1016/j.matdes.2013.10.064

DOI 10.12776/ams.v25i3.1290 p-ISSN 1335-1532
e-ISSN 1338-1156

[13] C. M. Lin, H. L. Tsai, C. D. Cheng, C. Yang: Engineering Failure Analysis, Vol. 21, 2012, p. 9–20, http://dx.doi.org/10.1016/j.engfailanal.2011.11.014
[14] S. A. A. Akbari Mousavi, R. Miresmaeili: Journal of Materials Processing Technology Vol. 208, 2008, No. 1–3, No. 21, p. 383–394 http://dx.doi.org/10.1016/j.jmatprotec.2008.01.015
[15] Y. Minami, H. Kimura, Y. Ihara: Mat. Sci. Tech., Vol. 2, 1986, p. 795-806, http://dx.doi.org/10.1179/026708386790219697
[16] G. Maistro, PhD thesis, Low-temperature carburizing/nitriding of austenitic stainless steels, Chalmers University of Technology, Gothenburg, Sweden 2018
[17] S. Kozuh, M. Gogic, I. Kosec: Kovove Mater. Vol. 47, 2009, p. 253-262
[18] V. P. Kujanpaa: Met. Constr., Vol. 117, 1985, p. 40-46
[19] M. Jelani, Z. Li, Z. Shen, N.UI Hassan, M. Sardar: Metals, Vol. 8, 2018, No. 620, p.1-13 http://dx.doi.org/10.3390/met8080620

DOI 10.12776/ams.v25i3.1290 p-ISSN 1335-1532
e-ISSN 1338-1156

EFFECT OF SPRINGBACK IN DP980 ADVANCED HIGH STRENGTH STEEL ON PRODUCT PRECISION IN BENDING PROCESS

Le Thai Hung[1)], Vu Thi Dinh[1)], Doan Thi Phuong[1)], Le Trung Kien[1)]*
[1)] Hanoi University of Science and Technology, Hanoi, Vietnam

Received: 17.05.2019
Accepted: 30.07.2019

[*]Corresponding author: email: hung.lethai@hust.edu.vn, Tel.: +84 0944910639, Department of Materials Mechanics and Metals Forming, School of Materials Science and Engineering, Hanoi University of Science and Technology, Hanoi, Vietnam)

Abstract
Springback is a common phenomenon in sheet metal forming, in which the material undergoes an elastic recovery as applied loads are removed. Springback causes the forming shape to deviate from the intended design geometry. This phenomenon, which can be influenced by several factors, effects on both bending angle and bending curvature. The aim of this study is to determine the influence of different tool radius and the gap between punch and die on springback in bending of DP980 Advanced High-Strength Steels (AHSS) sheet. Experimental studies are combined with FEM method in commercial ABAQUS software to determine the bending angle after springback. To predict springback in bending process, the material properties are defined by Ludwik - Hollomon law, combined with the Hill'48 criterion. Experimental results are in good agreement with numerical simulations in case of bending in the rolling direction.

Keywords: Springback, advanced high strength steel (AHSS), DP980

1 Introduction

AHSS is gradually replacing conventional steel grades in the automotive industry because of their advanced properties such as improved formability, crash worthiness, low-mass, affordable cost and many environmental advantages [1, 2]. However, a wide application of AHSS in many potential auto body and structural parts is still limited due to challenges in formability [3]. In AHSS sheet forming, the most sensitive feature is the elastic recovery during unloading, i.e., springback, which has been widely researched since the 1990s. Many studies have analyzed and investigated the effect of parameters on the springback effect on various grades of AHSS [4-10]. The amount of springback is influenced by various process parameters, such as gap between punch and die, material thickness [4], forming force, tool radius [5-6], ratio between die radius and thickness [7], blank holder force [8], and material properties including sheet anisotropy, Young's modulus, strength coefficient, and strain hardening exponent [9]. Nowadays, the prediction of such forming defects using numerical simulation becomes a critical step and popular in modern industry, which allow reduction of traditional costly trial-and-error experiments. However, an accurate prediction of springback from numerical simulation is still challenging since the springback are affected by many factors including the boundary conditions [11-16]. Previous studies have primarily focused on springback effects in AHSS grades with tensile strength less than 800MPa [17, 18]. For AHSS grades with a tensile strength of more than

DOI 10.12776/ams.v25i3.1306 p-ISSN 1335-1532
e-ISSN 1338-1156

800 MPa, however, a few research has been conducted regarding composition, characteristics, and especially formability, although such material has been used to manufacture details such as body and frame in the automobile industry. In the present study, the focus is put on springback effect in bending process of DP980 steel, which possesses tensile strength more than 1000MPa. By applying simulations to practical problems, ABAQUS software predicts the amount of springback of DP980 sheet steel in bending when changing the process parameters: tool radius, R = 5mm and the gap between punch and die, $c = 1.1t \div 1.2t$, where t is thickness of the sheet. Steel sample exhibits work-hardening described by Ludwik – Hollomon law combined with Hill'48 anisotropic yield criteria. For general stress states, the Hill'48 criterion is the most widely used criterion since it is relatively simple, and its parameters can be determined easily using standard tensile tests in laboratory conditions. After obtaining simulation results, a measurement of the springback angle is performed using the graphics method. Experimental process is carried out to compare with simulation results in case of R = 5 mm, $c = 1.2t$, and bending in the rolling direction to find out their compatible.

2 Experimental procedure

Material

DP980 is dual-phase steel, which consists of a ferritic matrix containing a hard martensitic second phase in the form of islands. Chemical composition in percentage of DP980 steel is shown in **Table 1** [19].

Table 1 Chemical composition of DP980 steel

Alloying element (%)	C	Mn	Cr	Al	P	Mo	Ni	Si	Fe
DP980	0.107	2.59	0.975	0.0314	0.0148	0.0099	0.0111	0.0911	96

Mechanical properties of DP980 steel sheet are provided as [19]: Young's modulus E = 210 GPa; Yield stress σ_0 = 677 MPa; Ultimate tensile strength = 1026MPa, Strength coefficient K = 1542 MPa; Strain hardening exponent n = 0.1409.

FEM simulation of springback effect models

In this study, the commercial software ABAQUS is used to simulate the bending process and predict the amount of springback in DP980 steel.

Fig. 1 shows the geometry models for the bending process of a DP980 sheet in case of R = 5 mm and $c = 1.2t$. These geometry models consist of punch, die, and blank.

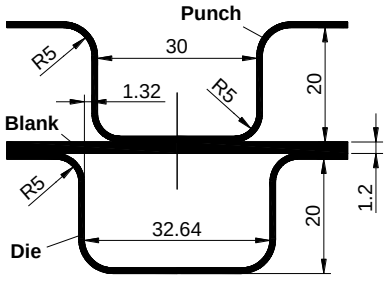

Fig. 1 Geometry model for forming simulation

DOI 10.12776/ams.v25i3.1306 p-ISSN 1335-1532
e-ISSN 1338-1156

To simulate the experiments, only one half of the specimen is modeled. The die and punch are modeled using the R3D4 rigid surface-elements, while the CPS4R elements are used for the blank. Throughout this study, the sizes of the blank are 90 mm (length) × 20 mm (width) × 1.2 mm (thickness).

The die is fixed in all directions. The punch is allowed to move only in the vertical direction. The deformation of the blank is restricted in transverse direction. The friction coefficient (μ) between the punch and the die is assumed of 0.1. The tool radius is R = 5 mm. The gap between punch and die is c = 10%.t. Photo map method is used to measure the springback level of DP980 AHSS sheet during bending process.

DP980 steel exhibits work-hardening described by Ludwik – Hollomon law combined with Hill'48 anisotropic yield criteria. These models are widely used because it is relatively simple, and its parameters can be determined easily using standard tensile tests in laboratory conditions.

The Ludwik – Hollomon equation is expressed as:

$$\sigma = \sigma_0 + K\varepsilon^n \tag{1.}$$

where K is strength coefficient, n is strain hardening exponent, and ε is true strain.

Since sheet material is commonly produced by cold rolling, the mechanical properties of material are thus different in the rolling direction (RD~xx), transverse direction (TD~yy), and normal direction (ND~zz). Therefore, anisotropic material properties are taken into account in the present study to investigate springback effect. The model of Hill'48 yield criteria is applied to describe the anisotropy properties of DP980 material. The Hill'48 equation is given by:

$$\varphi = F(\sigma_{yy} - \sigma_{zz})^2 + G(\sigma_{zz} - \sigma_{xx})^2 + H(\sigma_{xx} - \sigma_{yy})^2 + 2L\sigma_{yz}^2 + 2M\sigma_{xz}^2 + 2N\sigma_{xy}^2 = \bar{\sigma}^2 = Y_0^2 \tag{2.}$$

Where φ denotes the yield function, $\bar{\sigma}$ is the equivalent stress, and Y_0 a reference yield stress of the material. F, G, H, L, M and N are Hill's anisotropic parameters, which can be expressed by Lankford's coefficients with the condition $G + H = 1$ and plane stress condition $\sigma_{zz} = \sigma_{xz} = \sigma_{yz} = 0$. They are defined as

$$F = \frac{r_9}{r_{90}(r_0+1)}, N = \frac{(1+2r_{45})(r_0+r_{45})}{2r_{90}(1+r_0)}, L \text{ and } M \text{ are equal to } N. \tag{3.}$$

Where: r_0, r_{45}, r_{90} - Lankford's coefficients which represents anisotropy values measured in the 0°, 45° and 90° to the rolling direction, respectively, r_0 = 0,8354, r_{45} = 1,0347, r_{90} = 0,9441 [19] so F = 0,482111, G = 0,544836, N = 1,656289, H = 0,455164.

On the other hand, according to [20], they are also defined as

$$\begin{cases} F = \frac{1}{2R_{22}^2} + \frac{1}{2R_{33}^2} + \frac{1}{2R_{11}^2} \\ G = \frac{1}{2R_{11}^2} + \frac{1}{2R_{33}^2} + \frac{1}{2R_{22}^2} \\ H = \frac{1}{2R_{11}^2} + \frac{1}{2R_{22}^2} + \frac{1}{2R_{33}^2} \\ L = \frac{3}{2R_{23}^2}, M = \frac{3}{2R_{13}^2}, N = \frac{3}{2R_{12}^2} \end{cases} \tag{4.}$$

The anisotropic yield stress ratios R_{11}, R_{22}, R_{33}, R_{12}, R_{13} and R_{23} are obtained by above equation and given in **Table 2**.

DOI 10.12776/ams.v25i3.1306 p-ISSN 1335-1532
e-ISSN 1338-1156

Table 2 shows the anisotropic yield stress ratios

The anisotropic yield stress ratios	R_{11}	R_{22}	R_{33}	R_{12}	R_{13}	R_{23}
Values	1	1,067	0,974	0,952	1	1

Experimental conditions

DP980 sheet steels are cut under CNC K7745M machine with different directions compared to RD: 0°, 45°, and 90°, respectively. These specimens are then bent by MTS809 multifunctional machine (tensile testing machine) in case of R = 5 mm and c = 1.2t.

3 Results and discussion

Simulation results

Simulations that use the material model and the boundary conditions described in the previous section are performed by the means of ABAQUS software.

Fig. 2a shows the results of the bending process simulation in case of R = 5 mm, c = 1.2t.

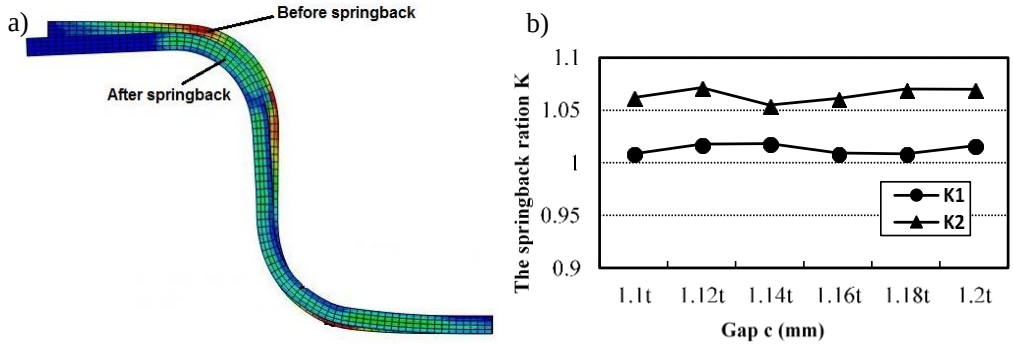

Fig. 2 a) The results of the bending process simulation in case of R = 5 mm, c = 1.2t; b) The springback ratio in various gap in case of R = 5 mm

To determine the springback amount, the angle after springback is firstly measured, then the springback ratio at the upper and bottom corners are calculated as $K_1 = \frac{\alpha_1}{\alpha}$ and $K_2 = \frac{\beta_1}{\beta}$, respectively. Where α, α_1 are upper corners before (expected =90^0) and after bending; β, β_1 are bottom corners before (expected =90^0) and after bending. The springback ratio in case of R = 5 mm is calculated at the upper corner K_1 and the bottom corner angle K_2. These calculation results are shown in **Fig. 2b.**

In case of R = 5 mm, both the upper and bottom corners are larger than 90 degrees. Thus, the smaller springback ratio is, the smaller the springback amount becomes. At the upper corner, the springback amount is the least in the case of c = 1.1t and the highest in case of c = 1.14t. And at the bottom corner, the springback amount achieves the lowest and highest values at c = 1.14t and c = 1.12t, respectively.

Based on the simulation results a few remarks may be given as follows: At the surveyed gap, different springback amounts are found at the upper and bottom corners.

To provide underlying mechanisms of occured springback effect, pairs of elements 1-2 and 3-4 are analyzed for stress-strain properties. These pairs of elements within the high stress region at the bending angle are symmetric across the neutral axis in the direction of the sheet thickness.

DOI 10.12776/ams.v25i3.1306 p-ISSN 1335-1532
e-ISSN 1338-1156

Pair of elements 1-2 are shown in **Fig. 3a**.

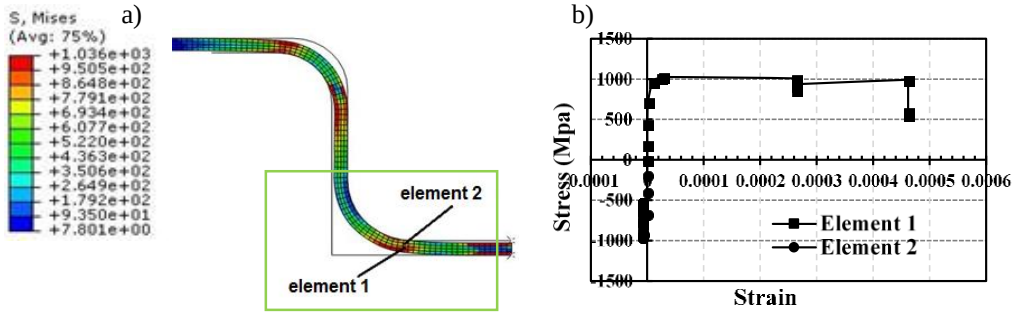

Fig. 3 a) Pair of elements 1-2; b) The principal stress-strain properties of elements 1 and 2

The principal stress-strain properties of elements 1 and 2 are shown in **Fig. 3b**.
The strain of element 2 is much smaller than that of element 1 along the bending process. Element 2 has a negative principal stress and strain while element 1 is positive. It proves that element 1 at the inner region of the bend is compressed while element 2 at the outer region is stretched and there is a difference in intensity of stress between these two elements.
The amount of principal stress and the principal stress and strain curve of elements 3 and 4 are shown in **Fig. 4a** and **Fig. 4b**.

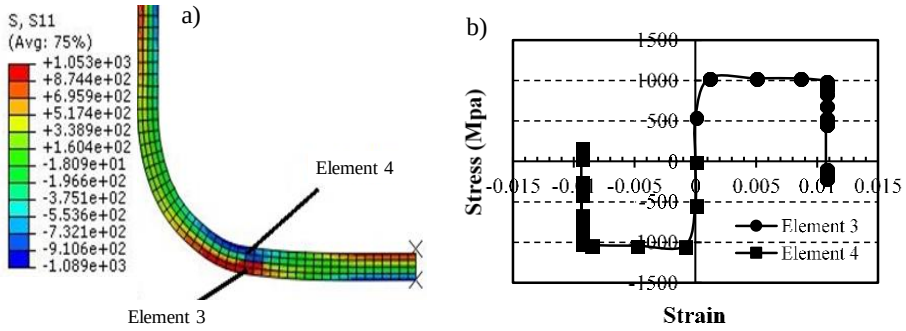

Fig. 4 a) The amount of principal stress in the blank; b) The principal stress and strain curve of elements 3 and 4

Similarly, element 4 is compressed while element 3 is stretched and there is a slight difference in intensity of stress between the two elements 3 and 4.
As the material is bent, the inner region of the bend is compressed while the outer region is stretched, so the molecular density is greater on the inside of the bend than on the outer surface. The compressive forces are less than the tensile forces on the outside of the bend. In addition, there is a difference in intensity of stress between two tensile and compression regions within the material. As a result, the material tends to return to its flat position.

Experimental results

Experimental results shown in **Fig. 5a** with different directions compared to RD: 0°, 45°, and 90°, respectively. To calculate the springback amount, the bending angles are measured. The obtained results are shown in **Fig. 5b**.

DOI 10.12776/ams.v25i3.1306 p-ISSN 1335-1532
e-ISSN 1338-1156

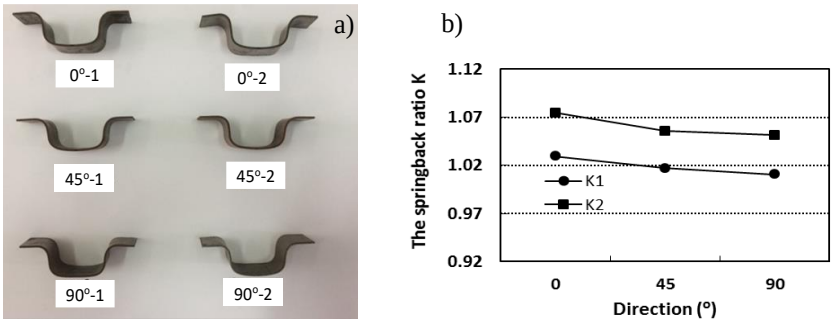

Fig. 5 a) Experimental results of specimens along 0°, 45°, 90° after forming in case of R = 5 mm and c = 1.2t; b) The sprinhback ratio of specimens along 0°, 45°, 90°

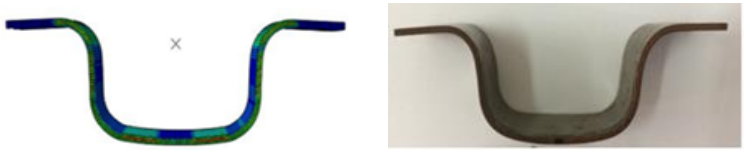

Simulation result Experimental result

Fig. 6 Simulation and experiment results comparison after bending that following the 0° directions

On the whole, the springback ratios in both the upper and bottom corners are greater than 1. Therefore, the higher the springback ratio is, the greater the springback amount becomes. The springback amount gradually decrease in three different directions 0°, 45°, 90° along with the rolling direction. **Fig.6** shows a comparison between simulation and experimental results after bending that following the 0° directions.

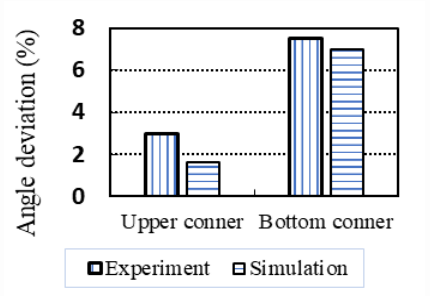

Fig. 7 Simulation and experiment angle deviation

Fig. 7 shows simulation and experiment angle deviation at the upper and bottom corners are less than 2.1%. This small value proves that the application of the hardening models is appropriate.

4 Conclusions

The simulation results shown that the springback amount of the DP980 steel varies in the upper and bottom corners according to the gaps. Where R = 5 mm, the largest springback percentage is 1.83 % in the upper corner and 7.14 % in the bottom corner.

DOI 10.12776/ams.v25i3.1306 p-ISSN 1335-1532
e-ISSN 1338-1156

Experimental results indicated that the springback amount gradually decreases in three different directions 0°, 45°, 90° along with the rolling direction. In the 0° direction, A comparison of simulation and experimental results showed that the springback amount of DP980 sheet steel at the bending angle after forming process is small. Therefore, the application of the hardening models for simulation is appropriate.

The results obtained from this study are the basis for calculating and selecting the solution when forming for DP980 AHSS.

References

[1] M. C. Theyssier: *Manufacturing of advanced high-strength steels (AHSS)*, Welding and Joining of Advanced High Strength Steels (AHSS), 2015, p. 29-53, https://doi.org/10.1016/B978-0-85709-436-0.00003-5

[2] T. B. Hilditch, T.de Souza, P. D. Hodgson: *Properties and automotive applications of advanced high-strength steels (AHSS)*, Welding and Joining of Advanced High Strength Steels (AHSS), 2015, p. 9-28, https://doi.org/10.1016/B978-0-85709-436-0.00002-3

[3] C. D. Horvath: *Advanced steels for lightweight automotive structures*, Welding and Joining of Advanced High Strength Steels (AHSS), 2015, p. 35-78, https://doi.org/10.1533/9781845697822.1.35

[4] A. Konieczny, M. Shi, C. Du: J of materials and manufacturing, Vol. 110, 2001, p. 1063-1067, https://doi.org/10.4271/2001-01-3106

[5] H. Chalal, S. G. Racz, T. Balan: Int J of Mechanical Sciences, Vol. 59, 2012, p. 104–114, https://doi.org/10.1016/j.ijmecsci.2012.03.011

[6] Bai, Y., Wierzbicki: *Predicting fracture of AHSS sheets on the punch and die radii and sidewall.* In: Proceedings of Numisheet, Interlaken, Switzerland, 2008, p. 297–306

[7] H. Lim, M. G. Lee, J. H. Sung, J. H. Kim, R. H. Wagoner: Int J Plast., vol.29, 2011, p. 42-59, https://doi.org/10.1016/j.ijplas.2011.07.008

[8] I. R and J. A. Nemes: SAE Technical Paper 2005-01-1332, 2005, p. 10, https://doi.org/10.4271/2005-01-1332

[9] X. Yang, C. Choi, N. K. Sever, T. Altan: International Journal of Mechanical Sciences, Vol. 105, 2016, p. 266-272, https://doi.org/10.1016/j.ijmecsci.2015.11.028

[10] R. H. Wagoner, H. Lim, M. - G. Lee: Int J Plast., Vol. 45, 2013, p. 3-20, https://10.1016/j.ijplas.2012.08.006

[11] D. M. Neto, M. C. Oliveira, A. D. Santos, J. L. Alves, L. F. Menezes: Int J Mech Sci, Vol. 122, 2017, p. 244-254, https://doi.org/10.1016/j.ijmecsci.2017.01.037

[12] Majidi, O., Barlat, F., & Lee, M.-G: Int J Mat Form, Vol. 9(3), 2015, p. 313–326, https://doi:10.1007/s12289-014-1214-7

[13] Leu, DK. & Zhuang, ZW: J Mech Sci Technol, Vol. 30(3), 2016, p. 1077-1084, https://doi.org/10.1007/s12206-016-0212-8

[14] Lee, J. W., Lee, M. G., & Barlat, F: Int J Plast, Vol. 29, 2012, p. 13-41, https://doi.org/10.1016/j.ijplas.2011.07.007

[15] D.T Nguyen, Y.S Kim, D.W Jung: Int J Precision Engineering And Manufacturing Vol. 13(8), 2012, p. 1425-1432, https://doi.org/10.1007/s12541-012-0187-z

[16] Angsuseranee, N & Pluphrach, G & Watcharasresomroeng, B & Songkroh, A: Songklanakarin J Sci. and Tech. Vol.40, 2018, p.534-539, 10.14456/sjst-psu.2018.87

[17] N. K Sever, O. H. Mete, Y. Demiralp, C. Choi, T. Altan, T: *Springback prediction in bending of AHSS-DP 780*, Proceedings of NAMRI/SME, Vol. 40, 2012, p. 94-103

DOI 10.12776/ams.v25i3.1306 p-ISSN 1335-1532
e-ISSN 1338-1156

[18] *S.A Abdullah, M.S. Buang, J.Saedon, H.Abdullah:* Journal Teknologi, Vol 76, No 3, 2015, p.69-72, https://doi.org/10.11113/jt.v76.5514

[19] H. T. Le, H. T. Nguyen: *Mechanical behavior of Advanced High Strength Steel of DP980*, Proceedings of the National conference on Mechanics, Duy Tan University, ISSN 978-604-913-458-6, 6-7/08/2015, p. 638-644

[20] D.T Nguyen, D.K Dinh, M.H.T Nguyen, T.L Banh, Y.S Kim: J. Cent. South Univ. Vol. 21, 2014, p. 27−34, https://doi.org/10.1007/s11771-014-1911-x

Acknowledgements

The authors would like to thank GIFT Postech and POSCO group for supply DP980 steel.

INFLUENCE OF RARE-EARTH ON THE MICROSTRUCTURE AND MECHANICAL PROPERTIES OF HIGH MANGANESE STEEL UNDER IMPACT LOAD

Duong Nam Nguyen[1)], Duong-Nguyen Nguyen[2], Mai Khanh Pham[3)]*
[1)] School of Mechanical Engineering, Vietnam Maritime University, Hai Phong, Vietnam
[2)] Japan Advanced Institute of Science and Technology, 1-1 Asahidai, Nomi, Ishikawa 923-1292, Japan
[3)] School of Materials Science and Engineering, Hanoi University of Science and Technology, Hanoi, Vietnam

Received: 21.05.2019
Accepted: 09.09.2019

[*]Corresponding author: e-mail: khanh.phammai@hust.edu.vn, Tel.: +840983030011, School of Materials Science and Engineering, Hanoi University of Science and Technology, No. 1, Dai Co Viet, Hai Ba Trung, Hanoi, Vietnam.

Abstract
In this paper, the influence of rare earth (RE) on the microstructure and mechanical properties of austenitic high manganese steel (HMnS) Mn15Cr2V were investigated. The results showed that the microstructure, hardness and impact strength of RE modification sample is finer and better than non-modified sample. Under the effect of impact load, the hardness and the depth of the work-hardening layer of the modified steel was higher than that of the non-modified steel, thereby, the value of microhardness in the surface of the modified sample was 420 HV while it was only 395 HV in the non-modified sample. The value of the impact strength of the modified sample was up to 132J/cm^2 compared to the non-modified sample is only 115J/cm^2. Moreover, after impact load, the austenite nanoparticles had been found out on the surface of this steel, this is the cause of the increasing of mechanical properties in this steel.

Keywords: austenite nanoparticles, rare earth, grain size, subzero temperature

1 Introduction

The high manganese steel has particularly resistant to abrasion when working under impact conditions, under the influence of stress. Under the effect of continuous working (such as sandblasting), the steel is abrasive relatively quickly, as other steel. After casting and heat treatment, the microstructure of its has austenite, which contains carbon and manganese. This steel has a high manganese content (over 10% Mn) [1-5]. Manganese is an element of γ expansion, so the steel is austenitic (stable austenite at room temperature). This steel has full the austenitic phase so the steel has high toughness, low hardness, but when working under high pressure and impact, the austenite particle (type A1 lattice) becomes strong plastic deformation. As a result, the steel/the hardness property of the steel becomes strong, while the core retains the original microstructure maintain the toughness. This phenomenon of high manganese steel is called "deformation" [6-15].

Rare earth (RE) are rare elements in the earth, including 17 elements: Scandium, Yttrium, Lanthanum... These elements are difficult to fabricate. Researchers have shown that putting rare earth on steel will have a small effect on the structure and increase the impact strength of the

DOI 10.12776/ams.v25i3.1309 p-ISSN 1335-1532
e-ISSN 1338-1156

material. In addition, RE elements can also be used as deoxygenators and desulfurizers as they are readily oxidized to RE oxides of RE. During crystallization, the compound of RE decomposes in front of the austenite crystal. After passing through an instantanous cooling process, they produce polycrystalline crystals instead of single crystals and under such conditions, several austenitic ions bind together and prevent crystallization of the crystals. Thus, they promote the same crystal growth and smooth the structure [16, 17].

The steel is alloyed by alloy elements as: Cr; V... M_7C_3 crystals size is larger than crystalline raddie than crystalline radii, reducing the length. However, the development of M_7C_3 is preferentially along the [0001] direction, so it is difficult to change the morphology. For this reason, the need for smoothing M_7C_3 bundles has been heavily researched. Rare earth elements are active surface elements, concentrated on a solid-liquid interface, which speeds up the cooling and inhibits the growth rate of austenite. When the first crystals of austenite appeared, they were bridged between carbide and austenite boundaries. The austenitic stalk branches connect together at the time the carbides become discrete and the shape of the carbide also changes from plate to plate or into rods [16, 18-20].

In this work, we present the results of the study on the effect of rare earth on the microstructure and mechanical properties of austenitic high manganese steel under impact load. The results proved that the HMnS steel with RE modification archive higher strengthen in comparison with other type of steel and the work-hardening mechanism was also changed as the old mechanism.

2 Experimental produre

In this research, the samples were melted in the induction furnace, the detail of chemical composition was shown in **Table 1**.

Table 1 Chemical composition of the samples

Sample	Fe	C	Si	Mn	P	S	Cr	V	RE
No.1	80.30	1.36	0.81	14.70	0.08	0.02	1.82	1.02	-
No.2	80.30	1.36	0.81	14.70	0.08	0.02	1.82	1.02	RE

The samples then processing of heat treatment as following: heating up to 650°C, keep at this temperature for 02 hours, air cooling down to room temperature, then were heated up to 1100°C and holding at that temperature for 02 hours, finally were water quenching.

The experiment samples were carried out under the impact load. Samples were applied more than 3000 times by load of 100N/cm^2 from the high of 60cm for observation of microstructure and hardness of specimens after applied impact load. The value of needed force is bigger than 439.5 MPa. The hardness was determined by Hardness tester ARK600. The microstructures were observed by Axiovert 25A, SEM QUANTA 250, XRD and TEM.

3 Results and discussion

3.1. Microstructure

Fig. 1 and **Fig. 2** shows the microstructure of the non-modified steels (**Fig. 1a**) and modified by rare earths (**Fig. 1b**). Samples have a V content of 1%, unmodified with an equivalent grade 5 equivalent grained ASTM. It can be seen that rare earth oxides with high melting temperatures cause heterogeneous crystallization of M_7C_3 carbide phase and austenite phase.

DOI 10.12776/ams.v25i3.1309 p-ISSN 1335-1532
e-ISSN 1338-1156

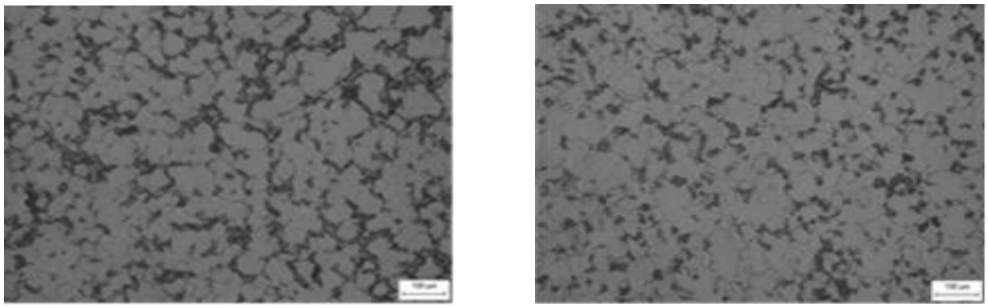

a) Sample 1 b) Sample 2

Fig. 1 Microstructure of non-modified sample (a) and modified sample (b) after casting

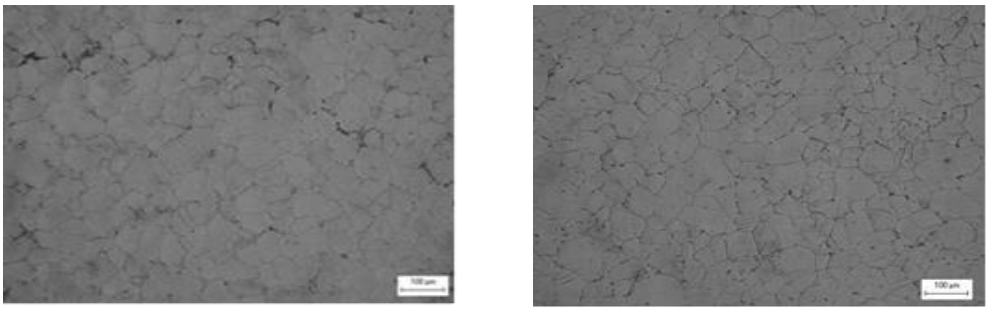

a) Sample 1 b) Sample 2

Fig. 2 Microstructure of non-modified sample (a) and modified sample (b) afterheat treatment

On **Fig. 2**, It can be seen that both of the modified and non-modified samples, the carbide particles of both the modified and non-modified samples have completely dissolved the carbide particles have completely dissolved into the austenite matrix and the austenitic particle size reaches grade 6 in accordance with ASTM. However, the modified sample is more uniform than the non-modified sample.

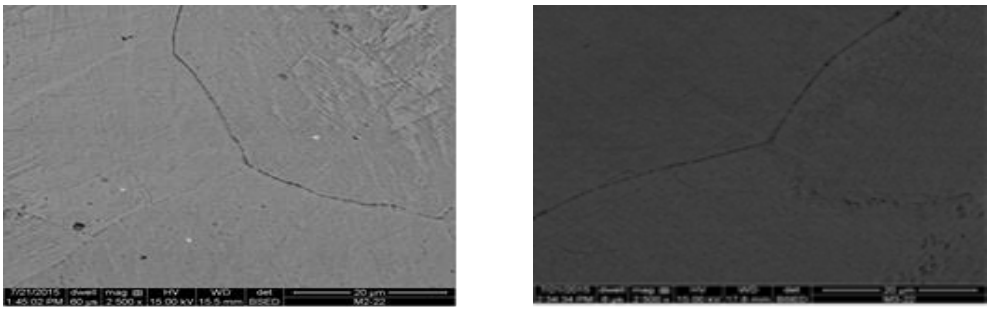

Sample 1 b) Sample 2

Fig. 3 BSE of non-modified sample (a) and modified sample (b) after heat treatment

The **Fig. 3a** shows the inverse scattering image of the non-modified sample after heat treatment. **Fig. 3b** is the modified sample's image after heat treatment. As in the microstructure,

DOI 10.12776/ams.v25i3.1309 p-ISSN 1335-1532
e-ISSN 1338-1156

backscattering electron images also showed that in the samples there was no concentration of carbide at the grain boundary (**Fig. 3b**), but in the austenitic granules there were appearance of a number of fine particles. The treatment of carbide dispersion within the austenitic matrix will contribute to the increasing of resistance to wear and impact toughness of the HMnS steel.

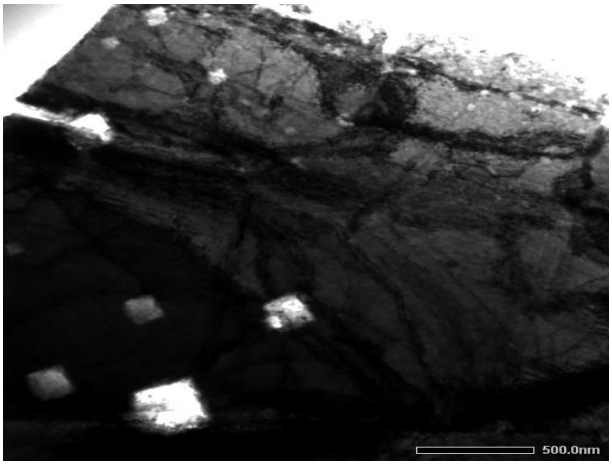

Fig. 4 Microstructure of TEM

From the observation of the optical image, in the microstructure of steel after heat treatment, almost all homogeneous austenite formed, only the use of TEM can show that there are carbide particles inside the austenitic particles. The size of these particles are very small. **Fig. 4** is the TEM image of the samples after heat treatment. From observations of the modified and non-modified samples by the TEM images, the small particles with approximate 60 nm in diameter length were observed with the non-modified and about 40 nm for the denominator (**Fig. 4**). These particles are playing the role of work hardening and abrasion resistance for the details. With the modified sample, the smaller finer particles appeared which increase the mechanical value compare than the non-modified sample.

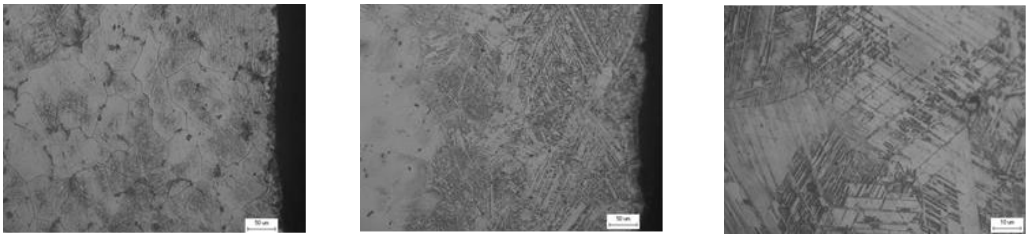

Sample 1 Sample 2 Sample 2 x1000

Fig. 5 Microstructure of non-modified sample 1 (a) and modified sample 2 (b;c)

The microstructure in **Fig. 5** shows that no martensitic structure can observed (**Figs. 5a** and **5b**). At the magnification of 1000 times, the twinning deformation can be seen in the microstructure of modified sample (**Fig. 5c**).

On the **Fig. 6**, the hardness of sample 2 is the higher than sample1 (hardness reaches 420HV). The results of TEM analysis of the samples after impacted load did not show the martensitic

DOI 10.12776/ams.v25i3.1309 p-ISSN 1335-1532
e-ISSN 1338-1156

structure for both samples, but only the nano scale level. However, by TEM, unlike the non-modified sample 1 (**Fig. 6a**), the modified sample 2 (**Fig. 6b**) appear strange appearance microstructure with many white dots. According to the author [16], austenite nanoparticles were created by plastic deformation (white dots in **Fig. 6b**). Thus, the deformation creates the austenite nanoparticles. The formation of austenite nanoparticles on the surface will increase the durability by creating multiple boundaries that prevent slippage and create differently oriented twinning. In addition, the fine grain increase the impact strength of this steel.

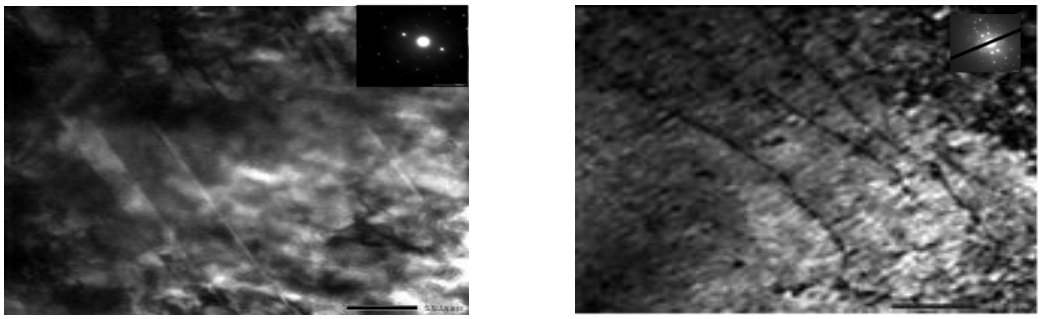

a) Sample 1 b) Sample 2

Fig. 6 Microstructure of non-modified sample 1 (a) and modified sample 2 (b)

Fig. 7 shows the inner surface of the sample 2 after the deformation process the sliding (**Fig. 7a**) are located at a distance of about 150 μm below the impact surface the impact surface where high hardness region is found (the maximum is 420HV). The deeper into the sample from the impact surface can be observed that the number of deviations decreases.

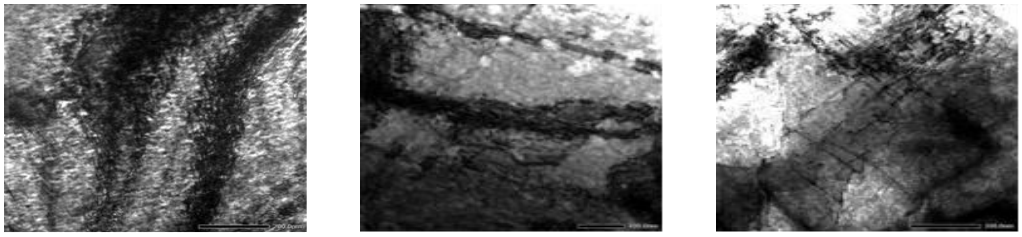

a) Sliding b) Sliding c) Dislocation

Fig. 7 Dislocation and sliding on the sample surface

3.2. Mechanical properties

The results of hardness samples (**Table 2**) showed that the modified samples exhibited higher hardness values than non-modified samples (240HB vs 223HB). This may explain the effect of the RE elements which increases the hardness value of the sample after heat treatment.

Table 2 Result of hardness

Sample	Hardness
Sample 1	223HB
Sample 2	240HB

DOI 10.12776/ams.v25i3.1309 p-ISSN 1335-1532
e-ISSN 1338-1156

Table 3 Result of impact toughness

Samples	Impact toughness (J/cm^2)
Sample 1	115
Sample 2	132

The results of the impact toughness showed that when the modified sample was performed with the heat treatment process as above, the impact toughness was higher than non-modified sample (132 J/cm^2 vs 115 J/cm^2). The value of impact toughness is increased by the particle size of the modified sample decrease. It can be indicated that RE elements were playing the important role not only in the solidification process, but also during in the heat treatment, which contributes to the reduction of austenitic grain size, thus improving the impact toughness of the samples.

Table 4 Abrasion of sample

Sample	Sample 1 (1%V)			Sample 2 (1%V+RE)		
	Begin	End	Mass loss weight	Begin	End	Mass loss weight
Weight (g)	4.7150	4.3590	0.3560	4.5320	4.3960	0.1360

The results in **Table 4** show the same abrasion test parametter as described in the experimental section: the sample, when added by rare earths, decreased the amount of wear compare than the untreated sample. Microstructures as well as mechanical properties analysis results of the samples are explained by the fact that RE elements were created the dislocation in the lattice and then promote to increase the mechanical properties of the samples.

Micro-hardness

In **Fig. 8**, the result is the micro-hardness which measured from the sample surface to the core. From the result of the hardness, it can be seen that at the same treatment temperature, the modified (S2) has a higher hardness value than the non-modified (S1) sample. At the room temperatures, the surface hardness of S2 reaches 420HV while the S1 is 395HV. This micro-hardness results show the role of the modification agent in the work-hardening of HMnS steel. Modifiers, which play the role in the austenite grain size reduction process, can also affected on the formation of strengthen phase in this steel.

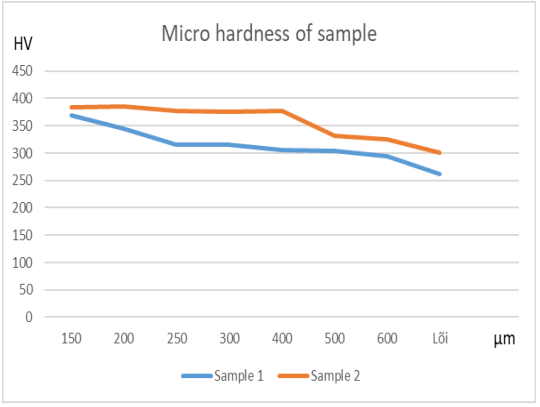

Fig. 8 Microhardness of sample

Fig. 8 shows that for the region locating at the distance of 120 μm below the surface, the hardness value has a greater slope than the inside two samples. It can be commented that apart from durable elements such as particle size, carbide particles may also have the role of austenite nanoparticles produced by austenite particles. The modified sample S2 has stable hardness at great distances (about 400μm). The depth and the value of hardening layers of sample 2 which will increase the wear resistance and impact toughness of this steel, is larger than the sample 1.

4 Conclusions

The results of the impact strength showed that when the samples were modified by RE and applied to the heat treatment process as above, the impact strength was 132 J/cm^2 higher than 115 J/cm^2 of the non-modified sample. This suggests that the role of the modifier in particle size reduction and the mechanical properties of this steel. The RE elements were greatly affected on the reduction of particle size, increasing the impact toughness of this steel.

The micro-hardness of the modified sample is higher than that of the non-modified sample (420HV is denatured compared to 395HV). Under the impact load, the microstructure of this steel have sliding, dislocation and nanoparticles. This structure were created by plastic deformation and austenite nanoparticles.

References

[1] C. Mahlami, X. Pan: *Mechanical properties and microstructure evaluation of high manganese steel alloyed with vanadium,* International Conference on Functional Materials, Characerization, Solid State Physics, Power, Thermal and Combustion Energy, India, AIP Coference Proceedings, Vol. 1859, July 2017, No. 1, https://doi.org/10.1063/1.4990236

[2] A. A. Gulyaev, Yu. D. Tyapkin, V. A. Golikov, V.S. Zharinova: Metal Science and Heat Treatment, Vol. 27, 1985, No. 6, p. 411-415, https://doi.org/10.1007/BF00693279

[3] X. Y. Feng, F. C. Zhang, Z. N. Yang, M. Zhang: Wear, Vol. 305, 2013, p. 299-304, http://dx.doi.org/10.1016/j.wear.2012.11.038

[4] W-S. Lee, T-H. Chen: Journal of Mechanical Engineering Science, Vol. 216, 2002, p. 971-982, https://doi.org/10.1243/095440602760400940

[5] U. Xu, L. Fang, Q. Cen, J. Zhu: Materials Science Forum, Vol. 475 – 479, 2005, p. 117-120, https://doi.org/10.4028/www.scientific.net/MSF.475-479.117

[6] J. Xie, Q. Jiang, Z. He, Q. Luo and K. Sommer: Journal of Materials Sciences and Technology, Vol. 8, 2009, p. 406-410

[7] N. D. Nguyen, C. T. Le, K. M. Pham: Key Engineering Materials, Vol. 737, 2017, p. 32-37, https://doi.org/10.4028/www.scientific.net/KEM.737.32

[8] N. D. Nguyen, C. T. Le, T. M. Nguyen, K. M. Pham*:* International Journal of Scientific and Engineering Research, Vol. 7, 2016, No. 4, p. 141-147

[9] R. Bidulsky, E. Hryha, J. Bidulska: High Temperature Materials and Processes, Vol. 35, 2016, No. 9, p. 865-870, https://doi.org/10.1515/htmp-2015-0107

[10] K. Q. Dang, Y. N. Nguyen, Q. A. Hoang, H. V. Tran, M. C. Nguyen, H. V. Pham, H. M. Le: Acta Metallurgica Slovaca, Vol. 24, 2018, No. 4, p. 273-279, http://dx.doi.org/10.12776/ams.v24i4.1195

[11] Q. Cen, Y. H. Xu, L. Fang, J. H. Zhu: Materials Science Forum, Vol. 475-479, 2005, p. 4187-4190, http://dx.doi.org/10.4028/www.scientific.net/MSF.475-479.4187

[12] B. Hutchinson, N. Ridley: Scripta Materialia, Vol. 55, 2006, No. 4, p. 299-302, http://dx.doi.org/10.1016/j.scriptamat.2006.05.002

[13] E. Dudrová, M. Kabátová, R. Bureš, R. Bidulský, A.S. Wronski: Kovove Materialy, Vol. 43, 2005, No. 6, p. 404-421
[14] C. Efstathiou, H. Sehitoglu: Acta Materialia, Vol. 58, 2010, No. 5, p. 1479-1488, http://dx.doi.org/10.1016/j.actamat.2009.10.054
[15] F. Haakonsen: *Optimizing of Strømhard austenitic manganese steel*, Thesis for the degree of Philosophiae Doctor, Norwegian University of Science and Technology, 2009
[16] J. Yang, F. Hao, D. Li, Y. Zhou, X. Ren, Y. Yang, Q. Yang: Journal of Rare Earths (English Edition), Vol 30, 2012, No. 8, p. 814-819, https://doi.org/10.1016/S1002-0721(12)60136-7
[17] K. M. Pham, N. D. Nguyen, C. T. Le, Q. N. T. Hoang: Materials Science Forum, Vol 804, 2014, p. 297-300, https://doi.org/10.4028/www.scientific.net/MSF.804.297
[18] K. M. Pham, N. D. Nguyen, T. A. Hoang: International Journal of Mechanical & Mechatronics Engineering, Vol. 18, 2018, No. 2, p. 141-147
[19] Z. Shi, M. Gu, J. Liu, Y. Yin: Journal of Materials Science and Technology, Vol. 11, 1995, No. 2, p. 102-108
[20] A. Pribulova, J. Babic, D. Baricova: Chemicke Listy, Vol. 105, 2011, p. 430-432

DOI 10.12776/ams.v25i3.1309 p-ISSN 1335-1532
e-ISSN 1338-1156

INDENTATION SIZE EFFECT OF HEAT TREATED ALUMINUM ALLOY

Jozef Petrík[1)], Peter Blaško[1)], Andrea Vasilňaková[1)], Peter Demeter[1)], Peter Futaš[1)]*
[1)] *Technical University of Košice, Faculty of Materials, Metallurgy and Recycling, Košice, Slovakia*

Received: 09.07.2019
Accepted: 23.09.2019

[*]*Corresponding author: e-mail:* jozef.petrik@tuke.sk, *Tel.: +421 55 602 2872, Institute of Materials and Quality Engineering, Faculty of Materials, Metallurgy and Recycling, Technical University of Košice, Letná 9, 042 00 Košice*.

Abstract
The aim of the submitted work is to study the influence of applied loads ranging from 0.09807 N to 0.9807 N on measured values of micro-hardness of heat treated aluminum alloy 6082. The influence of applied load on a measured value of micro-hardness was evaluated by Meyer's index n, PSR method and by Analysis of Variance (ANOVA). The influence of the load on the measured value of micro-hardness is statistically significant and the relationship between the applied load and micro-hardness manifests the moderate reverse ISE. As the temperature of the solution treatment rises, the YS/UTS ratio and also Meyer's index n, measured and "true hardness" increase. On the other hand, its effect on the plastic properties of the alloy is ambiguous.

Keywords: annealing, aluminium alloys, micro-hardness, ISE

1 Introduction

Aluminum alloys have been more and more extensively utilized in structural applications, aircraft, building and automotive industry due to their light weight and attractive mechanical properties achieved by heat treatment. In the Al-Mg-Si alloys the precipitation during aging after solution heat treatment and quenching significantly increase hardness and tensile strength.

Indentation hardness testing is a convenient means of investigating the mechanical properties of a small volume of materials. The principle of the Vickers micro-hardness method is identical to the macro-hardness test, except for considerably smaller test loads. It is frequently used for the determination of hardness of small items or thin layers [1].

In contrast to the (macro)hardness, it is well known that the apparent micro-hardness of solids depends on the load. This phenomenon, the indentation size effect (ISE), usually involves a modification in the apparent micro-hardness with a tenvariation of the load [2, 3].

If a very low load is used, the measured micro-hardness is usually high; with an increase in test load, the measured micro-hardness decreases. Such a phenomenon is sometimes referred to as "normal" ISE. Undoubtedly, the existence of the ISE may hamper or preclude plausible micro-hardness measurements [4]. The "normal" ISE may be caused by the testing equipment [1, 4, 5], the intrinsic structural factors of the material, load to initiate plastic deformation, indentation elastic recovery, elastic resistance of the materials, the effect of indenter/specimen friction resistance and the effect of the grinding and polishing of sample [1, 3-6].

In contrast to the above "normal" ISE, a reverse (inverse) type of ISE (RISE), where the apparent micro-hardness increases with increasing load, is also known. It essentially takes place in materials with predominant plastic deformation. It can be explained as an effect of vibration, indenter

DOI 10.12776/ams.v25i3.1310 p-ISSN 1335-1532
e-ISSN 1338-1156

bluntness at low loads, the energy loss as a result of sample chipping around the indentation or the generation of the cracks during the loading [3].
The purpose of this paper is to evaluate the influence of the load on micro-hardness of heat treated Al alloy 6082 by Meyer's, PSR and modified PSR methods. The scientific work devoted to the study of the influence of heat treatment on ISE is rare. This also applies to wrought aluminum alloys which, after forming, often follow heat treatment. The measurement of hardness and especially of micro-hardness is a suitable method of determining their mechanical properties, which has minimal material requirements and minimally damages the final product.

2 Experimental materials and methods

The investigation has been carried out on the aluminum Si – Mg – Mn alloy EN 6082 (STN 42 4400) which chemical composition (in wt.%) is in **Table 1.**

Table 1 The chemical composition of the alloy used for investigation.

Si	Mg	Mn	Fe	Cu	Ti	Cr
1.00	0.66	0.54	0.20	<0.03	<0.02	<0.02

The samples used for heat treatment had the shape of the cylinder with a length of 100 mm and a diameter of 16 mm. The samples were, after the solution treatment at temperatures listen in Table 2 with the holding time 3 hours quenched in the water. Then they were naturally aged for five days at 25°C. The sample No. 9 is the initial, hot extruded material used for heat treatment. One sample for the internaltensile test was turned for each temperature of the solution.
The temperature of heat treatment processes was measured by digital thermometer Testo 9010 with expanded uncertainty U = 2.3°C (k = 2) in calibration point 600°C.
The tensile test was carried out by the tester 200 kN Zwick-Extensometer according to standard ISO 6892-1:2016 [7]. The mean strain rate $\dot{e}_{Lc} = 0.024\ min^{-1}$. Results of the test are in **Table 2**.
The experimental error expressed as relative expanded uncertainty U_{rel} (coverage factor k = 2) is 1.82 % for values UTS and YS and less than 1% for values TE and Z. The YS/UTS ratio, which controls the local loss of plastic stability due to the internal structure of material (non-homogeneity, defects, but also due to the processing technology) for example in the deep-drawing process. High value of the ratio results in restricted formability and resistance to fatigue fracture on the other hand [8, 9]. As the temperature of the solution treatment rises, the YS/UTS ratio and also Meyer's index n increase.

Table 2 The temperature of the solution treatment, results of tensile test, (marco)hardness (HV10), micro-hardness (HV 0.05) and the relative expanded uncertainty of the hardness (U_{rel})

sample	T (°C)	UTS [MPa]	YS [MPa]	TE [%]	Z [%]	YS/UTS	HV10	U_{rel} HV10 [%]	HV0.05	U_{rel} HV0.05 [%]
1	590	235	131	20.4	26.7	0.557	118	7.6	118	15.0
2	580	237	121	19.5	44.5	0.511	122	7.7	111	18.0
3	570	242	124	23.8	46.9	0.512	121	6.9	114	15.3
4	560	230	126	20.8	51.4	0.548	117	7.6	134	13.1
5	550	236	124	19.6	51.8	0.525	124	8.7	110	15.9
6	540	314	127	15.6	43.9	0.404	108	7.5	107	17.0
7	530	298	144	16.0	42.8	0.483	102	7.6	101	17.5
8	520	280	143	13.2	48.9	0.511	95	8.4	98	18.3
9	-	291	113	18.8	47.2	0.388	105	5.8	103	17.0

DOI 10.12776/ams.v25i3.1310 p-ISSN 1335-1532
e-ISSN 1338-1156

A head part of the longer fractured tensile piece was used as a sample for metallographic analysis and measurement of the macro- and micro-hardness. The diameter of the piece was measured at regular intervals from the neck to the head. Dimensions parallel to the axis of the sample are measured with an accuracy 0.01 mm and dimensions perpendicular to the axis with an accuracy 0.001 mm.

The surface was wet ground on silicon carbide papers (the sequence 80, 120, 220, … 2500 and 3000 ANSI/CAMI grit) and mechanically polished with a water suspension of Al_2O_3 and then with diamond paste (0.5 μm) to a mirror finish. Samples were finally etched with water solution 0.5 % HF. The etching visualized hard intermetallic phases, firstly Al-Fe. The areas with the occurrence of intermetallic phases were avoided at micro-hardness measurement.

The microstructure was analyzed by optic microscope Neophot 32 in magnifications 500 × and 1000×, using the software ImageJ. The aluminum matrix contains fine intermetallic particles which became visible after etching. The area of their proportion is 1.8 % in the initial material and it is between 0.8 % and 1.3 % in heat treated samples. The temperature of the solution treatment did not significantly affect this proportion.

The (macro)hardness tests were performed by the equipment HBO 250. The magnification of the measuring device is 70×. The certified reference material (CRM) in the form of hardness reference block with specified hardness H_c = 194 HV 10 and expanded uncertainty U_{CRM} = 3.3 HV 10 (k = 2) was used as a standard for the calibration of the tester; it met the requirements of the standard ISO 6507-2:2018 [10] (the repeatability r_{rel} = 1.94%, the error of tester E_{rel} = 0.20 % and the expanded uncertainty of the calibration (k = 2) U_{rel} = 1.07 %). Measured values of the (macro)hardness are in **Table 2**.

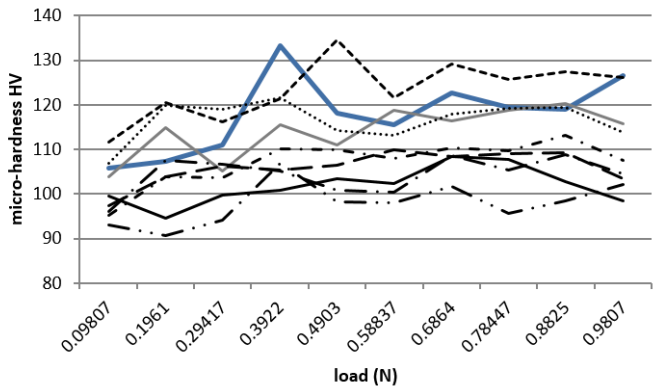

Fig. 1 The relationship between load and micro-hardness

Micro-hardness was measured by tester Hanemann, type Mod D32 fitted to microscope Neophot-32 with a magnification 480×. The discrimination - the value of the smallest division of the optical device, which measures the diagonals of the indentation, is 0.000313 mm.

A reference block – CRM (certified reference material) with specified hardness H_c = 195 HV0.05 and expanded uncertainty U_{CRM} = 8 HV 0.05 (k = 2) was used for the calibration of the micro-hardness tester; the tester meets the requirements of the standard ISO 6507-2:2018 [10] (r_{rel} = 4.39 %, E_{rel} = 3.81 % and U_{rel} = 9.01%).

Both macro- and micro-hardness were measured according to standard ISO 6507-1:2018 [11]. Applying load P for (macro)hardness was 98.07 N and loads for micro-hardness were between

DOI 10.12776/ams.v25i3.1310 p-ISSN 1335-1532
e-ISSN 1338-1156

0.09807 N and 0.9807 N by 0.09807 N step with application time 15 s. An operator performed five indentations at each load. For micro-hardness, the result was "the cluster" of 50 indentations, regularly distributed over the surface of the sample at one sample. If the measured micro-hardness was extremely high or the shape of the indentation was distorted, the indenter was likely contacted with the subsurface intermetallic phase. The measured value was not taken into account, and the measurement was repeated. The mean velocity of the micro-indenter in the sample, calculated by the method described in [12] was 1.0 μm s^{-1}. The values of micro-hardness, measured at particular loads are in **Fig. 1** and it at load 0.49 N (HV0.05) with its uncertainty are also in **Table 2**. As can be seen, the uncertainty of the micro-hardness is higher as it of (macro)hardness. It is the result of higher deviation of the diagonals of micro-indentations and at the same time higher uncertainty of used CRM (e. i. the ratio of CRM uncertainty and the hardness of tested aluminum alloy). The majority of samples manifest a moderate reverse indentation size effect (RISE). The ambient temperature in the laboratory ranged between 20.0 and 20.7 °C.

3 Results

According to two way analysis of variance (ANOVA, significance level $\alpha = 0.05$) without replication the load ($p = 3.52 \times 10^{-8}$) and the solution treatment temperature ($p = 6.32 \times 10^{-22}$) both have the statistically significant influence on the measured values of the micro-hardness.

Meyer's power law and proportional specimen resistance (PSR) are two principal approaches to describe ISE quantitatively [1].

The basic method to describe the ISE is Meyer's Law:

$$P = Ad^n \tag{1.}$$

Meyer's index n and the coefficient A (as A_{ln}) determined by the straight line graph of ln d (the mean diagonal of the indentation d in μm) versus ln P (the applied load P in g). Meyer's index n is the slope and coefficient A_{ln} is the y-intercept of the line.

Table 3 The ISE and PSR indices

method	Meyer's law		PSR		Modified PSR		
sample	n	A_{ln}	a_1 [N mm^{-1}]	a_2 [N mm^{-2}]	c_0 [N]	c_1[N mm^{-1}]	c_2 [N mm^{-2}]
1	2.1340	6.918	-1.686	690.08	0.0006	-1.677	689.06
2	2.1095	6.794	-1.559	662.82	0.0012	-1.722	666.68
3	2.0317	6.557	-0.100	621.03	-0.0421	3.635	548.08
4	2.1147	6.895	-1.458	711.51	-0.0326	1.455	653.41
5	2.1231	6.778	-1.355	618.36	-0.0543	3.157	534.63
6	2.0766	6.600	-0.676	586.11	-0.0787	5.824	466.64
7	2.0510	6.494	-0.541	572.17	0.0110	-1.412	587.68
8	2.0719	6.501	-0.787	546.11	-0.0183	0.708	519.19
9	2.0571	6.489	-0.615	560.98	-0.0903	6.650	430.71

However, as stated by a number of authors, for example, Sargent [13], presented the relationship between Meyer's index and work hardening coefficient was derived using the ball indenter. Unfortunately, it has become common practice to apply the strain-hardening Tabor interpretation to pyramidal indentation and to derive a "work-hardening index". The purpose of the contribution is not to give an opinion on whether the Meyer index is a measure of the work hardening coefficient or it is not. In this case, its task will only be to quantify the possible existence and magnitude of the relationship between load and microhardness, i.e. ISE.

DOI 10.12776/ams.v25i3.1310 p-ISSN 1335-1532
e-ISSN 1338-1156

The index n < 2 indicates "normal" and n > 2 indicates reverse ISE. If n = 2, the micro-hardness is independent of the load and is given by Kick's law.
The curves load/micro-hardness in **Fig. 1** show a non-linear increase of the micro-hardness with the applied load to 0.2942 – 0.4903N and then remain practically constant with further increasing of the load. This boundary of the stabilization as called as "ISE boundary". Calculated values of Meyer's index n and A_{ln} are in **Table 3**.
The proportional specimen resistance model of Li and Bradt (PSR) may be considered a modified form of the Hays/Kendall approach to the ISE [4]. Several authors [1, 4, 5, 14, 15] have proposed that the normal ISE may be described by the (2):

$$P = a_1 d + a_2 d^2 \tag{2.}$$

Li and Bradt pointed out that the parameters a_1 (N mm^{-1}) and a_2 (N mm^{-2}) of (2) are related to the elastic and plastic properties of the material, respectively [16].
The parameter a_1 characterizes the load dependence of micro-hardness and describes the ISE in the PSR model. It consists of two components: the elastic resistance of the test sample and the friction resistance developed at the indenter facet/sample interface [1, 5].
The parameter a_2 is directly related to the test sample's load-independent micro-hardness sometimes referred to as "true hardness" [4].
Equation (2) may be rearranged in the form:

$$\frac{P}{d} = a_1 + a_2 d \tag{3.}$$

The parameters a_1 and a_2 of (3) may be obtained from the plots of P/d (in N/mm) against d (in mm). Measured values of a_1 and a_2 are given in **Table 3**.
According to energy balance approach parameter c_0 is associated with residual surface stresses in the sample and parameters $c_1 \approx a_1$ and $c_2 \approx a_2$ are related, respectively with the elastic and plastic properties of the sample [1, 4].
Equation (4) can be regarded as a modified form of the PSR model.

$$P = c_0 + c_1 d + c_2 d^2 \tag{4.}$$

The parameters c_0 (N), c_1 (N mm^{-1}) and c_2 (N mm^{-2}) of (4) may be obtained from the quadratic regressions of P (in N) against d (in mm) and their measured values are given in **Table 3**.
The ratio c_1/c_2 (**Table 4**) is a measure of the residual stresses due to the machining and polishing of the sample while c_0 denotes the residual stresses in the sample. Therefore a relationship between c_0 and c_1/c_2 is expected [1], **Fig. 2**. With increasing macro and micro-hardness, the ratios a_1/a_2 and c_1/c_2 both decreases, c_0 and Meyer's index n increase.
Hays and Kendall proposed the existence of minimum test load W (N) necessary to initiate plastic deformation – the result is visible indentation. Only elastic deformation occurs below such load. In that event, the load dependence of hardness is expressed by equation (5):

$$P = W + A_1 d^2 \tag{5.}$$

Where A_1 (N mm^{-2}) is a constant independent of load. The values of W and A_1 may be obtained from the regressions of P (N) against d^2 (mm) [1]. The values of the indices obtained by modified PSR are given in **Table 4.** However, visible indentations (and so with plastic deformation) were created with the load 0.009807 N. This fact does not conform to the definition of parameter W.

DOI 10.12776/ams.v25i3.1310 p-ISSN 1335-1532
e-ISSN 1338-1156

Parameters a_2, c_2, and A_1 are directly related to load-independent micro-hardness sometimes referred to as "true hardness" H_{PSR} [1, 4, 5, 17].

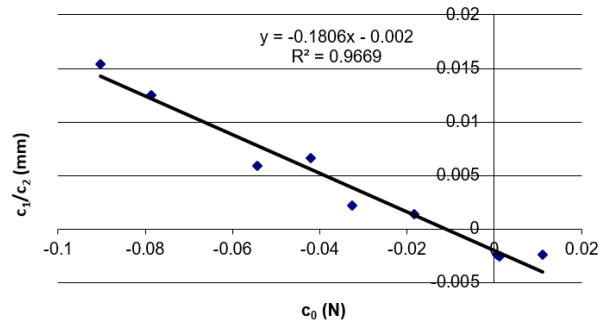

Fig. 2 The relationship between c_0 and c_1/c_2

$$H_{PSR}a_2 = 0.1891 \times a_2 \quad (6.)$$

The "true hardness" by analogy to a_2 can be calculated as H_{PSRA1} using A_1 and also $H_{PSR}c_2$ using c_2 in equation (6). The relationships between the ratio YS/UTS and "true hardness" calculated with the aid of the indices a_2, c_2 and A_1 and measured hardness HV0.05 and HV10 can be seen in **Fig. 3**. The coefficient of the determination R^2 ranged between 0.67 (for H_{PSRc2}) and 0.22 (for HV10).

Table 4 The ISE and PSR indices and "true hardness"

sample	W [N]	A1	c1/c2 [mm]	**H_{PSRa2}**	**H_{PSRc2}**	**H_{PSRA1}**
1	-0.0200	658.01	-0.002430	130.4941	130.3012	124.4297
2	-0.0203	635.31	-0.002580	125.3393	126.0692	120.1371
3	0.0030	614.37	0.006633	117.4368	103.6419	116.1774
4	-0.0150	680.84	0.002226	134.5465	123.5598	128.7468
5	-0.0133	589.97	0.005904	116.9319	101.0985	111.5633
6	-0.0024	567.59	0.012481	110.8334	88.24162	107.3313
7	-0.0074	563.09	-0.002400	108.1973	111.1303	106.4803
8	-0.0088	531.09	0.001364	103.2694	98.17883	100.4291
9	-0.0012	543.48	0.015440	106.0813	81.44726	102.7721

4 Discussion

Parameter c_0 is associated with residual surface stress in the sample. It was assumed that the head part of the sample, used for ISE evaluation would not be significantly deformed. As can be seen in **Table 4** a certain difference in residual surface stress was observed. However, the mentioned differences were smaller than they obtained on a sample of the same material on the places with different local reduction of the area (contraction). Since the relationship between c_0 and the temperature of the solution treatment is negligible ($R^2 = 0.04$), the differences are likely the result of residual strain (for example, different deformations of heads when attached to the grips of the tensile machine). The ratio c_1/c_2 is the measure of the residual stress due to machining and polishing. Individual samples were sawn, ground and polished under approximately the same conditions. However, certain differences, which could cause differences in the values of c_1/c_2 ratio may have occurred (for example the polishing time or the contact force in the polishing or grinding). Hays and Kendall defined the parameter was a minimum load necessary to initiate

DOI 10.12776/ams.v25i3.1310 p-ISSN 1335-1532
e-ISSN 1338-1156

plastic deformation, therefore a creating a visible indentation. However, visible indentations (and so with plastic deformation) were created with the load 0.009807N, which is less than some calculated values of parameter W listed in **Table 4**. This fact does not conform to the definition of parameter W. It would be appropriate to focus the research on both of these problems in the future.

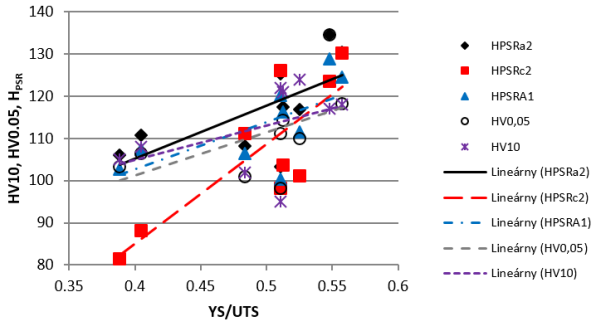

Fig. 3 The relationship between the YS/UTS ratio, "true hardness" HPSR and measured hardness HV0.05 and HV10

It is necessary to remember the fact that the indirect calibration of micro-hardness testers is not a routinely practiced process, unlike the (macro) hardness testers. We can determine the uncertainty of the measured micro-hardness only by the calibration. However, uncertainty can significantly affect the type and size of ISE. It is possible that "normal" and reverse ISE are simultaneously the result of the same input values if the uncertainty is taken into account (with a coverage factor k = 2) [18]. The ambiguity in the measurement of small indentations, particularly if pile-up or sink-in effects are present, can lead to over- or underestimation of diagonals [19, 20].

4 Conclusion

1. The influence of the load on the measured value of micro-hardness is statistically significant.
2. The relationship between the applied load and micro-hardness manifests moderate reverse ISE.
3. As the temperature of the solution treatment rises, the YS/UTS ratio and also Meyer's index n, measured and "true hardness" increase. On the other hand, its effect on the plastic properties of the alloy (reduction of the area Z and the elongation TS) is ambiguous.
4. The measured micro-hardness is effected by reverse ISE.

References

[1] K. Sangwal, B. Surowska, P. Błaziak: Materials Chemistry and Physics, Vol. 77, 2002, No. 2, p. 511-520, HTTPS://DOI.ORG/10.1016/S0254-0584(02)00086-X

[2] M. M. Yovanovich: *Micro and Macro Hardness Measurements, Correlations, and Contact Models*. In: 44th AIAA Aerospace Sciences Meeting and Exhibit, Reno, Nevada, 2006, http://www.mhtl.uwaterloo.ca/pdf_papers/mhtl06-2.pdf

[3] K. Sangwal: Materials Chemistry and Physics, Vol. 63, 2000, No. 2, p. 145-152, HTTPS://DOI.ORG/10.1016/S0254-0584(99)00216-3

[4] J. Gong, J. Wu, Zh. Guan: Journal of the European Ceramic Society, Vol. 19, 1999, No. 15, p. 2625-2631, https://doi.org/10.1016/S0955-2219(99)00043-6
[5] X. J. Ren, R. M. Hooper, C. Griffiths: Journal of Materials Science Letters, Vol. 22, 2003, No. 15, p. 1105-6, http://dx.doi.org/10.1023/A:1024947210604
[6] V. Navrátil, J. Novotná: Aplimat – Journal of Applied Mathematics. Vol. 2, 2009, No. 3, p. 241-244
[7] ISO 6892-1, Metallic materials - Tensile Testing. Part 1: Method of test at room temperature, ISO, Brussels, 2016
[8] A. Kováčová, T. Kvačkaj, R. Bidulský, J. Bidulská, R. Kočiško, J. Dutkiewicz, L. Lityńska-Dobrzyńska: Archives of Metallurgy and Materials, Vol. 62, 2017, Issue 2, p. 851-856, https://doi.org/10.1515/amm-2017-0125
[9] T. Kvačkaj, A. Kováčová, J. Bidulská, R. Bidulský, R. Kočiško: Archives of Metallurgy and Materials, Vol. 60, 2015, Issue 2A, p. 605-614, https://doi.org/10.1515/amm-2015-0180
[10] ISO 6507-2:2018 Metallic materials. Vickers hardness test. Part 2: Verification and calibration of testing, ISO, Brussels, 2018
[11] ISO 6507-1:20185 Metallic materials. Vickers hardness test. Part 1: Test method. ISO, Brussels, 2018
[12] J. Petrík, P. Palfy, P. Blaško, L. Girmanová, M. Havlík, Manufacturing technology. Journal for science, research and production Vol. 16, 2016, No. 4, p. 771-777, http://journal.strojirenskatechnologie.cz/templates/obalky_casopis/XVI_2016-4.pdf
[13] Ph. M. Sargent, Journal of materials science letters, Vol. 8, 1989, No. 10, p. 1139-1140, https://link.springer.com/article/10.1007/BF01730048
[14] H. Li, R. C. Bradt, Journal of Materials Science, Vol. 28, 1993, No. 4, p. 917-926, https://doi.org/10.1007/BF00400874
[15] B.D. Michels, G. H. Frischat, Journal of Materials Science, Vol. 17, 1982, No. 2, p. 329-334, https://doi.org/10.1007/BF00591466
[16] H. Kim, T. Kim, Journal of the European Ceramic Society, *Vol.* 22, 2002, No. 9-10, p**.** 1437-1445, https://doi.org/10.1016/s0955-2219(01)00457-5
[17] R. Machaka, T. E. Derry, I. Sigalas, M. Herrmann, Advances in Materials Science and Engineering, 2011, http://dx.doi.org/10.1155/2011/539252
[18] J. Petrik, P. Palfy: Metrology and measurement systems, Vol. 18, 2011, No. 2, p. 223-234, https://doi.org/10.2478/v10178-011-0005-5
[19] J. Petrík: Materials Science – Medžiagotyra, Vol. 20**,** 2014, No**.** 1, p. 21-24, http://dx.doi.org/10.5755/j01.ms.20.1.4017
[20] D. Tabor, Review of Physics in Technology, Vol. 1, 1970, No. 3, p. 145-179, https://doi.org/10.1088/0034-6683/1/3/I01

Acknowledgment
Authors are grateful for the support of experimental works by the project of the Slovak Grant Agency for Science VEGA 1/0073/17.

SYNTHESIS OF Cu_2ZnSnS_4 BY MECHANICAL ALLOYING METHOD FOR THERMOELECTRIC APPLICATION

Bui Duc Long[1)], Nguyen Van Khanh[1)], Duong Ngoc Binh[1)], Le Hong Thang[1)], Le Thi Bang[1)], Suhana Binti Mohd Said[2)]*

[1)]School of Materials Science andEngineering, Hanoi University of Science and Technology, No.1 Dai Co Viet, Hanoi, Vietnam

[2)]Department of Electrical Engineering, Faculty of Engineering, University of Malaya, Malaysia

Received: 21.05.2019
Accepted: 31.08.2019

[*]Corresponding author: email: long.buiduc@hust.edu.vn, Tel.:+84 24 3868 0355, School of Materials Science and Engineering, Hanoi University of Science and Technology, No.1, Dai Co Viet Street, Hai Ba Trung, Hanoi, Vietnam

Abstract

Quaternary chalcogenide Cu_2ZnSnS_4 is a potential candidate for thermoelectric (TE) application due to a number of advantages including containing only non-toxic and abundant elements, high Seebeck coefficient and low thermal conductivity. In this study, Cu_2ZnSnS_4 was synthesized using mechanical alloying method from Cu, Zn, Sn and S powders. In order to study the effect of milling duration on the formation of Cu_2ZnSnS_4, different milling duration of 2, 4, 12 and 16 h were carried out. As the results, Cu_2ZnSnS_4 wasstarted to form after milling for 12 h. The formation of Cu_2ZnSnS_4 was completed after 16 h of milling. In addition, Cu_2ZnSnS_4 nanoparticles were obtained after 16 h of milling with the particle distribution mostly in the range of 50 - 60 nm.

Keywords: Mechanical alloying; Cu_2ZnSnS_4; Thermoelectric;Powder metallurgy

1 Introduction

Alarming environment and energy crisis associated with insatiable demand of energy from fossil fuel sources,which has resulted in efforts of seeking clean and sustainable energy sources. It has been estimated that two-thirds of the primary energy from fossil fuels consumed by humans is wasted, with mostof it being waste heat[1-3]. The recovery of huge amount of wasted heat not only has a significant influence on the efficiency of energy consumption,but also reduces the global greenhouse gas emission.Thermoelectric generators (TEGs), which are capable of generating electricity directly from waste heat sources by Seebeck effect,have emerged as a novel technology for recovering waste heats from automobiles, industrial sectors and home cooking etc. TEGs are solid-state devices, which areholding a number of advantages over conventional powder generators, such as silent operation,no moving parts, reliable durabilityand no gas emission [4-6]. However, currently TEGs still exist some main drawbacks including low efficiency and high cost of TE materials, which are primary factors restricting for large-scale applications [7-9].

The performance of a type of TE materials is evaluated by the dimensionless figure of merit *ZT*, ($ZT = \sigma S^2T/\kappa$, where S,σ, κ are Seebeckcoefficient, electrical conductivity and thermal conductivity, respectively). T is the absolute average temperature between the hot and the cold sides of TEGs. A high efficiency TE material, therefore, should possess a high Seebeck

DOI 10.12776/ams.v25i3.1311 p-ISSN 1335-1532
e-ISSN 1338-1156

coef*fi*cient(S), high electrical conductivity (σ) in combination with low thermal conductivity (κ). Although the commercial TE materials have a ZT value of 1.0, however, TE devices require a ZT of 3.0 to be a competitive candidate in practical applications [10].

Among potential TE materials studied for middle range temperature application, quaternary chalcogenide Cu_2ZnSnS_4 (CZTS) has recently received a great interestfrom scientist due high stability in air, high melting temperature, low thermal conductivity, high Seebeck coefficient, and particularly containing only non-toxic and earth abundant elements [11, 12].The synthesis of CZTS has been studied through a number of methods, such as, sputtering [13], thermal evaporation [14], solution phase reaction [15], sol–gel [16] and spray pyrolysis [17]. However, these methods either require particular equipment for complicated process and low production mass. Hence, it is challenging to develop facile and cost-effective methods, which are capable oflarge-scale production.

In this study, kesterite CZTSwas synthesized using a simple method which is mechanical alloyingofCu, Zn, Sn and Spowders. The formations of CZTS, morphology and particle sizes of milled powders were investigated.

2 Experimental procedure

For preparation of CZTS precursor, Cu (99.5%,−100 mesh, Strem Chemicals), Zn(99.9%,−325 mesh, Strem Chemicals), Sn (99.5%, −100 mesh, Alfa Aesar), and S (99.5%, −325 mesh, Alfa Aesar) powders were used as starting materials. Mixtures of powders with the stoichiometric ratio of 2:1:1:4 were milled using Fritsch Planetary Mono Mill Pulverisette 6 classic line for various milling durations of 2, 4, 12and 16h under Ar atmosphere. The ball to powder ratio and the milling speed were of 10:1 and 300 rpm, respectively. In order to minimize contamination of milled powders, the mill media and container were made of zirconia oxideand no process control agents were added into the mixtures.

The phase transformation after ball milling was analyzed using X-ray diffractometer (Bruker D8 Advance, CuKαradiation, 1.54059 Å). The surface morphologies of the mixed powders and milled powders were studied by field-emission scanning electron microscope (FE-SEM) (Hitachi S-4800).For particle size distribution analysis, random 50 particles from each image were measured using ImageJ software.

3 Results and discussion

In the present work, the effect of milling duration on the phase transformation of milled CZTS powders was investigated by using differentmilling duration of 2, 4, 12and16 h, whilst other parameters remained constant. The XRD patterns of a raw mixture of Cu, Zn, Sn and S powders, and milled powders are shown in **Fig. 1**.

The XRD pattern of the mixedpowder shows a number of sharp peaks attributed to the elemental powders of Cu, Zn, Sn and S. After 2 h and 4 h of milling, the XRD peaks of elemental powders of Cu, Zn, Sn and S were broadened and the intensity of peaks was decreased due to the refinement of the crystallites and the increase in lattice strain [18]whilst no obvious peaks of CZTS appeared.After milling for 12 h, most XRD peaks of the starting powders disappeared except a peak of Cu. Besides, it can be seen that four primary peaks were appeared, which are attributed to the diffraction of the planes (112) (200) (220) (312) of CZTS. This indicates that the formation of CZTS has been taken place. After a prolonged milled duration of 16 h, all peaks of elemental powders were disappeared, whilst there were only peaks of CZTS present. The

DOI 10.12776/ams.v25i3.1311 p-ISSN 1335-1532
e-ISSN 1338-1156

crystal structure of CZTS has been completed with the appearance of primary peak attributed to the planes (332). It can be concluded that the mixture of powders has been mechanically alloyed completely after 16 h of milling.The formation of CZTS in our experiment was taken place in a shorter milling duration compared to which were reported by Pareek *et al.*[19]and Wang *et al.*[20]. Pareek *et al.* reported that pure CZTS was synthesized completely from starting elemental powders after ball milling for 30 h with the rotation speed of 450 rpm andthe ball-to-powder weight ratio of 5:1, whilst Wang *et al.* reported that the formation of CZTS was completed after milling for 20 h at 50 Hz frequency with the rotation speed of 300 rpm and at the same ball-to-powder weight ratio of 5:1. These above mentioned differences could be primarily attributed to the differences in milling process variables including ball-to-powder weight ratio, model of milling machine, the molar ratio of elemental powders and the particle sizes of powders (the manufacturers of the source powders are different in the present work and the literatures).

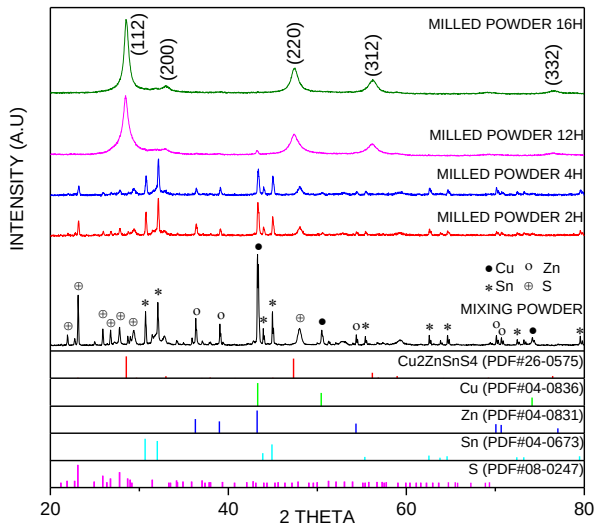

Fig. 1 XRD patterns of mixing powder and milled powders at different duration

During ball mill, the mixture of powder particles is repeatedly flattened, cold-welded, fractured and rewelded. The formation mechanism of CZTS during high-energy ball mill is attributed tothe diffusion process, which takes place when particles are cold-welded together. Heavy plastic deformations during milling createa variety of crystal defects such asdislocations, vacancies, stacking faults, and increasethe grain boundaries, and so, enhances the diffusion process.In addition, slightly temperature raise during milling further aids the diffusion process; consequently, true compound is formed.The specific times required to develop a given structure in any system depends on the initial particle size, characteristics of the ingredients,and the operating parameters of the equipment [21-23].

There is an important characteristic to be noted in the XRD data of milled powders after 12 h and 16 h of milling that is a slight peak shift to lower or higher 2θ values in the samples, which corresponds with result reported in previous paper [19]. This phenomenon can be due to the presence of a large amount of defects, lattice strain and disorder, which usually results in peak shift, in milled powders after a long milling duration, as seen in **Fig. 2**.

DOI 10.12776/ams.v25i3.1311 p-ISSN 1335-1532
e-ISSN 1338-1156

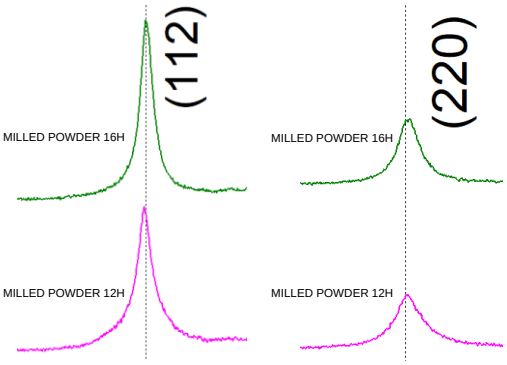

Fig. 2 Zoomed-in of XRD pattern of two main peaks of milled powders in small ranges of 2θ (left) from 25 to 30° and (right) from 45 to 50°

Morphologies of the mixture powders before and after milling at different duration were investigated using SEM, as shown in **Fig. 3**. It can be seen in **Fig. 3 (a)** that particles of raw element powders separated completely or loosely contact which can be observed clearly in distinguishable shape. However, the powder particles started to be plastically deformed and get cold-welded after 2 h of milling although some un-welded particles still existed, as illustrated in **Fig. 3 (b)**. After 4 h of milling, the cold-welding and fracturing processes continued to take place leading to microstructural refinement, as shown in **Fig. 3 (c)**. At this milling duration, the distribution of particle sizes can be observed in a large range.

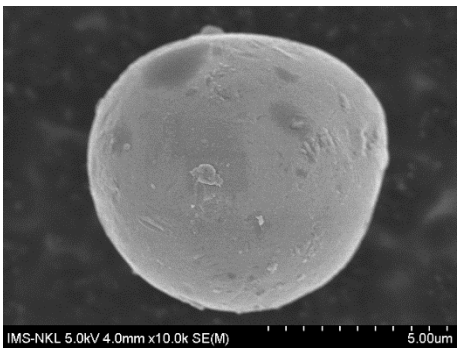

(a)

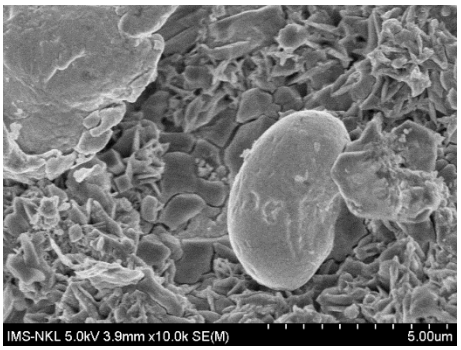

(b)

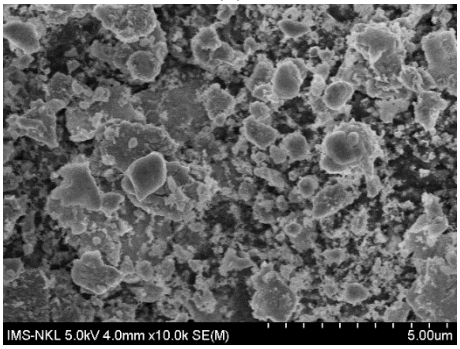

(c)

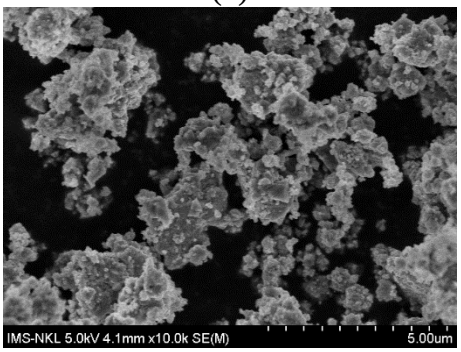

(d)

DOI 10.12776/ams.v25i3.1311
p-ISSN 1335-1532
e-ISSN 1338-1156

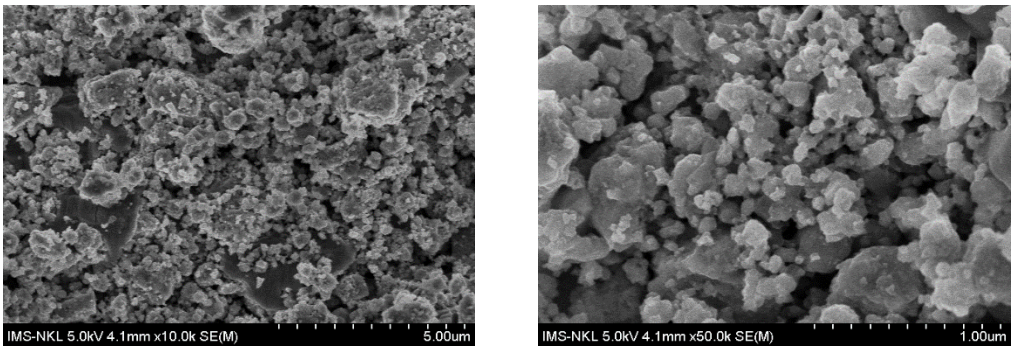

(e) (f)

Fig. 3 SEM morphologies of (a) raw powder mixture and milled powders after (b) 2 h, (c) 4 h, (d) 12 h and (e) 16 h of milling. Image (f) is SEM morphology of 16 h milling with high magnification (50,000 X)

After milling for long duration of 12 h and 16 h, the particles continued to cold-weld and fracture but the tendency to fracture predominates over cold-welding. As the results,numbers of small particles wereincreased, **Fig. 3 (d),(e)**. With high magnification SEM image (**Fig. 3(f)**), it can be clearly seen that the powder particles of 16 h milling became round shapes and the distribution of particle sizes is mostly in the range of 50 - 60 nm, as seen in **Fig. 4**.

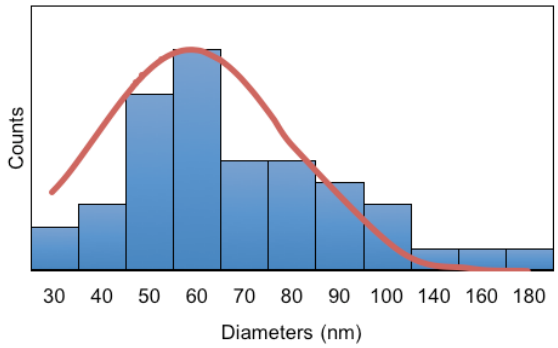

Fig. 4 The distribution of particle size of milled CZTS after 16 h milling

4 Conclusions

In this research, kesterite CZTS was synthesized using mechanical alloying method from Cu, Zn, Sn and S powders. After milling of 12 h, the CZTS phase was formed. Single phase of CZTS was obtained completely after 16 h of milling. The milled powderswere obtainedin nanosized with the particle distribution mostly in the range of 50 - 60 nm after 16 h of milling.

References

[1] R. Ovik, B. D. Long, M. C. Barma, M. Riaz, M. F. M. Sabri, S. M. Said, R. Saidur: Renewable & Sustainable Energy Reviews, Vol. 64, 2016, p. 635–659, http://dx.doi.org/10.1016/j.rser.2016.06.035

[2] X. Zhang, L.D. Zhao: Journal of Materiomics Vol.1, 2015, p. 92-105, http://dx.doi.org/10.1016/j.jmat.2015.01.001

[3] Y. Wu, S.W. Finefrock, H. Yang: Nano Energy Vol. 1, p. 651-653, http://dx.doi.org/10.1016/j.nanoen.2012.08.001
[4] C. R. S. Rodrigues, T. Machado, A. L. Pires, B. Chaves, F. S. Carpinteiroa, A. M. Pereira: Applied Thermal Engineering, Vol. 138, 2018, p. 319–324, http://dx.doi.org/10.1016/j.applthermaleng.2018.04.046
[5] S. LeBlanc: Sustainable Materials and Technologies Vol.1–2, 2014, p. 26–35, https://doi.org/10.1016/j.susmat.2014.11.002
[6] G. J. Snyder, E. S. Toberer, Nature, Vol. 7, 2008, p. 105-114, http://dx.doi.org/10.1038/nmat2090
[7] T. Kvackaj, R. Bidulsky, A. Kovacova, J. Ileninova, J. Bidulska: Acta Metallurgica Slovaca, Vol. 20, 2014, No. 4, p. 397-404, https://doi.org/10.12776/ams.v20i4.438
[8] W. He, G. Zhang, X. X. Zhang, J. Ji, G. Li, X. Zhao: Applied Energy Vol. 143, 2015, p. 1-25, https://doi.org/10.1016/j.apenergy.2014.12.075
[9] M. Ibańez et al.: Chemistry Materials, Vol. 24, 2012, p. 562−570, http://dx.doi.org/10.1021/cm2031812
[10] X. Zhang, L. D. Zhao: Journal ofMateriomics, Vol. 1, 2015, p. 92-105, http://dx.doi.org/10.1016/j.jmat.2015.01.001
[11] M. L. Liu, F. Q. Huang, L. D. Chen, I. W. Chen: Applied Physics Letter, 94, 2009, p. 202103, http://dx.doi.org/10.1063/1.3130718
[12] A. Nagaoka, T. Masuda, S. Yasui, T. Taniyama, Y. Nose: Applied Physics Express, Vol. 11, 2018, p.051203, https://doi.org/10.7567/APEX.11.051203
[13] T. P. Dhakal, C. Peng, R. Reid Tobias, R. Dasharathy, C. R. Westgate: Solar Energy, Vol. 100, 2014, p. 23–30, http://dx.doi.org/10.1016/j.solener.2013.11.035
[14] C. Shi, G. Shi, Z. Chen, P. Yang, and M. Yao: Materials Letters, Vol. 73, 2012, p. 89–91, http://dx.doi.org/10.1016/j.matlet.2012.01.018
[15] H. Yang, L. A. Jauregui, G. Zhang, Y. P. Chen, and Y. Wu: Nano Letters, Vol. 12, No. 2, 2012, p. 540–545, http://dx.doi.org/10.1021/nl201718z
[16] B. L. Guo, Y. H. Chen, X. J. Liu, W. C. Liu, A. D. Li: AIP Advance, Vol. 4, No. 9, 2014, p. 097115, http://dx.doi.org/10.1063/1.4895520
[17] M. Aono, K. Yoshitake, H. Miyazaki: Physica Status Solidi (c), Vol. 10, No. 7–8, Aug. 2013, p. 1058–1061, http://dx.doi.org/10.1002/pssc.201200796
[18] C. Suryanarayana: Progress in Materials Science, Vol. 46, No. 1–2, 2001, p. 1–184, http://dx.doi.org/10.1016/S0079-6425(99)00010-9
[19] D. Pareek, K. R. Balasubramaniam, P. Sharma: Materials Characterization, Vol. 103, 2015, p. 42–49, http://dx.doi.org/10.1016/j.matchar.2015.03.014
[20] Y. Wang and H. Gong: Journal of Alloys Compounds, Vol. 509, No. 40, 2011, p. 9627–9630, http://dx.doi.org/10.1016/j.jallcom.2011.07.041
[21] C. Suryanarayana: Progress in Materials Science, Vol. 46, 2001, p. 1-184, https://doi.org/10.1016/S0079-6425(99)00010-9
[22] M. Besterci, F. Dobeš, T. Kvačkaj, K. Sülleiová, B. Ballóková,O. Velgosová, Acta Metallurgica Slovaca, Vol. 20, 2014, No. 3, p. 326-340, http://dx.doi.org/10.12776/ams.v20i3.307
[23] T. Kvackaj, A. Kovacova, J. Bidulska, R. Bidulsky, R. Kocisko: Archives of Metallurgy and Materials, Vol. 60, 2015, No. 2A, p. 605-614, https://doi.org/10.1515/amm-2015-0180

Acknowledgements

This work is supported by National Foundation for Science and Technology Development (Nafosted), grant No.103.02-2016.18.

STUDY OF $M_{23}C_6$ PRECIPITATION IN A 45Ni-35Cr-Nb ALLOY

Matías Humberto Sosa Lissarrague[1,2)], Alejandro Sepulveda Buitrago[3)], Alberto Carlos Picasso[2,4)]*

[1)] IFISUR, Universidad Nacional del Sur, CONICET, Departamento de Física - UNS, Av. L. N. Alem 1253, B8000CPB, Bahía Blanca, Argentina

[2)] Laboratorio de Metalurgia y Tecnología Mecánica, Universidad Nacional del Sur, Departamento de Ingeniería, Av. L. N. Alem 1253, B8000CPB, Bahía Blanca, Argentina

[3)] Universidad Pontificia Bolivariana, Kilómetro 7 vía Piedecuesta, 680001, Bucaramanga, Colombia

[4)] Comisión de Investigaciones Científicas de la Provincia de Buenos Aires (CICPBA), Calle 526 entre 10 y 11, B1900, La Plata, Argentina

Received: 25.06.2019
Accepted: 06.09.2019

[*]Corresponding author: e-mail: mhsl1986@gmail.com, Tel.: +54 0291 4595179, Laboratorio de Metalurgia y Tecnología Mecánica, Universidad Nacional del Sur, Departamento de Ingeniería, Av. L. N. Alem 1253, B8000CPB, Bahía Blanca, Argentina

Abstract

The 45Ni-35Cr-Nb alloy, commonly known as ET45 micro, produced in the form of centrifugally cast tubes, was studied by means of optical microscopy after aging treatments at 1073 and 1173 K for different times. A description of $M_{23}C_6$ secondary carbides precipitation phenomenon was made as a function of time. The purpose of carrying out a kinetic study of the precipitation of this phase is to be able to calculate the activation energy required for secondary precipitation. This allows to infer what is the mechanism associated with it. Analysis after using the Johnson-Mehl-Avrami-Kolmogorov (JMAK) model showed that secondary carbide precipitation occurs in a single stage. It was found that this phenomenon, which is assisted by diffusion, has an activation energy of 196 kJ/mol. This value would indicate that the diffusion of Cr atoms in the austenitic matrix is the phenomenon that dominates the precipitation of the $M_{23}C_6$ secondary carbide.

Keywords: JMAK model, 45Ni-35Cr-Nb alloy, secondary carbide precipitation, aging

1 Introduction

ET45 micro centrifugal cast alloy is commonly applied in pyrolysis furnaces used in petrochemical industry being able to operate between 973 and 1373 K. The resistance to carburization is influenced by the stability of austenite, which in turn depends on the Cr and Ni concentration ratio. High concentrations of Cr and Ni, prevent the diffusion of C from the external atmosphere into the alloy [1-9]. To achieve high mechanical strength and creep resistance during high temperature service, Nb, Ti, Zr are added to those alloys. In addition, the presence of Si and Mn increases the resistant of the alloy under aggressive atmospheres [10, 11]. The dendritic-type microstructure of the alloy consists of an austenitic matrix strengthened by a network of primary carbides that increases its mechanical strength. During service at high temperatures, fine intradendritic Cr-rich $M_{23}C_6$ secondary carbides precipitate within the matrix, increasing mechanical properties and improving the stability of the phases precipitated in the microstructure [4,5]. Therefore, it is interesting to analyse the mechanism of precipitation, as well as what

DOI 10.12776/ams.v25i3.1312 p-ISSN 1335-1532
e-ISSN 1338-1156

elements or chemical compounds are involved in it. The kinetic model proposed by Johnson, Mehl, Avrami and Kolmogorov (JMAK model) is commonly used in the kinetic study of nucleation and growth reactions, the precipitation of new phases linked to a diffusive process [12], recrystallization [13], ferroelectric/ferromagnetic switching [14], and surface growth in gas/vacuum environments [15]. For this reason, JMAK kinetic model will be applied for the study of the secondary precipitation of Cr-rich $M_{23}C_6$ carbides.

2 Experimental

Chemical composition of the 45Ni-35Cr-Nb heat resistant alloy is shown in **Table 1**.

Table 1 Chemical composition of centrifugally cast alloy ET45 micro [wt %]

C	Si	Mn	Ni	Cr	Fe	Nb	Ti + Zr
0.45	1.60	1.00	45.00	35.00	16.00	1.00	<0.09

The alloy was produced as centrifugally cast pipes, with a 110 mm diameter and 11 mm wall thickness. Specimens of cast material were obtained from a ring extracted of the tube and cut transversely with a 12 mm width.

Aging heat treatment was made at 1073 and 1173 K using resistive furnaces in air atmosphere. For each temperature, aging times were of 1, 5, 15 and 30 min, and 1, 3, 8, 16, 24 and 27 h. After aging, each specimen was cooled in air. Metallographic preparation was done with abrasive sheet papers of decreasing particle size, electrolytic etching was carried out with a KOH 10% aqueous solution, applying a voltage of 2 V during 14 s. Optical micrographs were taken using a Leica optical microscope model DM ILM equipped with a DFC 295CCD camera. Finally, area fraction of secondary carbides was measured by image analysis using ImageJ software version 1.41, developed by National Institutes of Health in the United States of America. This software is based on the contrast of colors between an object and the background in order to measure the ratio between the area occupied by the objects whose color contrasts with the color of the background, and the total area of the image. Area fraction values were measured by optical microscopy with a magnification of 1000X on each sample for each temperature.

3 Results and discussion

Applying JMAK model, it can be obtained the transformed fraction of a new phase, f, as a function of time. This model is exactly accurate for nucleation and growth reactions with linear growth, while it is a good approximation in cases of nucleation and growth with parabolic growth, i.e. as in the case of diffusion-controlled growth. The hypotheses that this model must satisfy be valid, include random distribution of the precipitated phase, isotropic growth, average growth rate is uniform throughout the material, precipitation reaction is not influenced by time-dependent processes, and the amount of a phase that can be transformed is independent of time [11, 16, 17]. In this case, it is a thermally activated phenomenon controlled by diffusion. Therefore, the Avrami exponent and the activation energy should remain constant while the transformation occurs. For random nucleation, that means that nuclei formation is independent of the position on the volume sample, and for the case of linear growth, the JMAK model presents an exact fit for any value of f [18]. The Avrami equation, relates the transformed fraction with aging time by:

$$f = 1 - \exp(-k.t)^n \quad (1.)$$

DOI 10.12776/ams.v25i3.1312 p-ISSN 1335-1532
e-ISSN 1338-1156

where: f - area fraction of secondary carbides
n - Avrami exponent
k [s^{-1}] - pre-exponential factor
t [s] - aging time

The pre-exponential factor, k, is defined by an Arrhenius-type equation as:

$$k = k_0 . \exp\left(-\frac{Q}{R.T}\right) \quad (2.)$$

where: k_0 [s^{-1}] - constant
Q [kJ/mol] - activation energy of deformation
R [kJ/(K·mol)] - universal gas constant
T [K] - temperature

From the Avrami equation it is possible to obtain the following equation, which corresponds to a straight line of slope n and intercept n.ln(k). In **Fig. 1**, it is shown the plot of this straight line as a function of ln(t) for each one of the aging temperatures.

$$\ln(-\ln(1-f)) = n.\ln(t) + n\,.\ln(k) \quad (3.)$$

For 1073 K, the equation of the fitting function is:

$$\ln(-\ln(1-f)) = 0.88.\ln(t) - 8.29 \quad (4.)$$

In such a way, for 1173 K, the equation is:

$$\ln(-\ln(1-f)) = 0.78.\ln(t) - 6.42 \quad (5.)$$

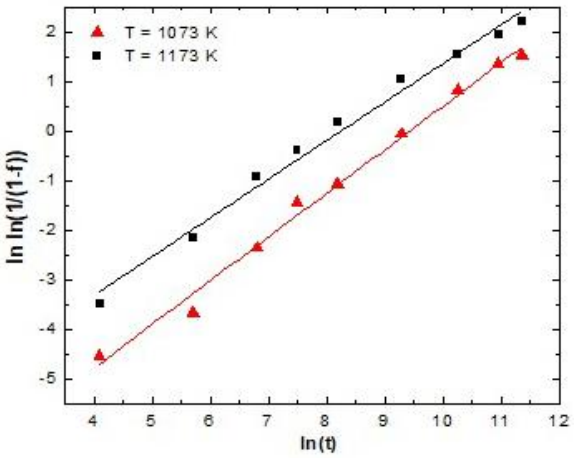

Fig. 1 Linear adjustment using the Avrami equation vs. aging time

Unlike what other authors have found for similar alloys [19], in this work the evolution of secondary carbides precipitation was characterized by having only one step. Once the parameters of the Avrami equation for each aging temperature have been calculated, it is possible to compare the experimental data of the transformed fraction with those represented by the kinetic model, as it is shown in **Fig. 2**.

DOI 10.12776/ams.v25i3.1312 p-ISSN 1335-1532
e-ISSN 1338-1156

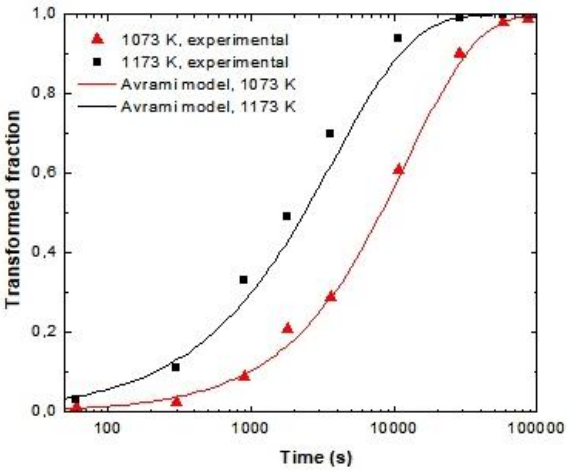

Fig. 2 Evolution of the experimental and calculated transformed fraction vs. aging time

By plotting n.ln(k) vs. $(R.T)^{-1}$ as it is shown in **Fig. 3**, it can be obtained a straight line of slope Q and intercept $\ln(k_0)$:

$$\ln(k) = \ln(k_0) - \frac{Q}{R.T} \quad (6.)$$

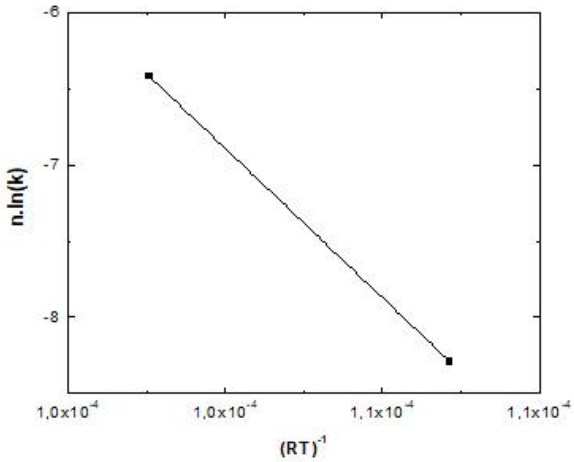

Fig. 3 Evolution of ln(k) vs. $(R.T)^{-1}$ in order to calculate the activation energy.

In this way, the calculated activation energy Q of secondary $M_{23}C_6$ carbides precipitation is 196 kJ/mol and the intercept of this straight line is 13.64 so k_0 is $8.39x10^6$ s^{-1}. The activation energy Q of the secondary precipitation reaction, allows identifying the mechanism that dominates the precipitation of $M_{23}C_6$ carbides. In this case, as it is a phenomenon assisted by diffusion, it is important to know the activation energy for self-diffusion of atoms that make up the secondary precipitates, that is, C and Cr. In the case of C, the self-diffusion energy in an austenitic matrix is of 142 kJ/mol [20] while some authors have found using an experimental procedure similar to that used in this work, activation energy of 213 kJ/mol for a Fe-30.8Ni-26.6Cr alloy [19]. The latter,

DOI 10.12776/ams.v25i3.1312 p-ISSN 1335-1532
e-ISSN 1338-1156

turns out to be of the order of the calculated from the model of JMAK for the alloy under study, which would indicate that the mechanism that controls the secondary precipitation is the diffusion of the Cr atom.

4 Conclusions

From the kinetic analysis by the classical Johnson-Mehl-Avrami-Kolmogorov model of secondary carbides precipitation in a 45Ni-35Cr-Nb heat resistant alloy, it is possible to reach the following conclusions. First, it was found that the phenomenon occurs in a single stage, and the calculated activation energy is 196 kJ/mol. The activation energy obtained is comparable to that corresponding to the self-diffusion of Cr in an austenitic matrix in alloys of the Ni-Cr-Fe type similar to the one studied on this work. For this reason, the diffusion of Cr through the austenitic matrix would be the mechanism that controls the formation of $M_{23}C_6$-type secondary Cr-rich carbides. The study and analysis of the evolution of the precipitation process, shows that n parameter remains almost constant with aging temperature.

References

[1] X. Zhang, D. Kong: Scientific Journal of Material Science, Vol. 3, 2013, No. 4, p. 124-127
[2] J. Laigo, F. Christien, R. Le Gall, F. Tancret, J. Furtado: Material Characterization, Vol. 59, 2008, p. 1580–1586, http://dx.doi.org/10.1016/j.matchar.2008.02.001
[3] K. Buchaman, M. Kral, C. Bishop: Metallurgical and Materials Transactions A, Vol. 45, 2014, p. 3373–3385, https://doi.org/10.1007/s11661-014-2285-2
[4] I. Sustaita Torres et al.: Materials Chemistry and Physics, Vol. 133, 2012, p. 1018-1023, https://doi.org/10.1016/j.matchemphys.2012.02.010
[5] A. Picasso, C. Lanz, M. Sosa Lissarrague, A. Garófoli: Journal of Minerals and Materials Characterization and Engineering, Vol. 4, 2016, p. 48-61, https://doi.org/10.4236/jmmce.2016.41006
[6] R. Song, S. Wu: Engineering Failure Analysis, Vol. 88, 2018, p. 63-72, https://doi.org/10.1016/j.engfailanal.2018.01.002
[7] A. Reihani, R. Derakhshandeh Haghighi: Engineering Failure Analysis, Vol. 52, 2015, p. 97-108, https://doi.org/10.1016/j.engfailanal.2015.03.005
[8] E. Kenik, P. Maziasz, R. Swindeman, J. Cervenka, D. May: Scripta Materialia, Vol. 49, 2003, p. 117–122, doi: https://doi.org/10.1016/S1359-6462(03)00238-0
[9] C. Liu, X. Chen, T. Chen, X. Lian, J. Sun: Procedia Engineering, Vol. 130, 2015, p. 693-700, https://doi.org/10.1013/j.proeng.2015.12.165
[10] G. Barbabela, L. de Almeida, T. da Silveira, I Le May: Material Characterization, Vol. 26, 1991, p. 193-197
[11] H. Khatak, B. Raj: *Corrosion of austenitic stainless steel: mechanism, migration and monitoring*, first ed., Alpha Science International Ltd., Pangbourne, 2012
[12] R. Badji et al.: Materials Chemistry and Physics, Vol. 148, 2014, p. 664-672, https://doi.org/10.1016/j.matchemphys.2014.08.032
[13] I. Shimizu: Philosophical Magazine A, Vol. 79, 1999, p. 1217-1231, https://doi.org/10.1080/01418619908210357
[14] R. Ramos, P. Rikvold, M. Novotny: Physical Review B, Vol. 59, 1999, p. 9053-9069, https://doi.org/10.1103/PhysRevB.59.9053
[15] O. Becker: The Journal of Chemical Physics, Vol. 96, 1992, p. 5488-5496, https://doi.org/10.1063/1.462704

DOI 10.12776/ams.v25i3.1312 p-ISSN 1335-1532
e-ISSN 1338-1156

[16] F. Liu, P. Sommer, C. Boss, E. Mittemeijer: International Materials Reviews, Vol. 52, No. 4, 2007, p. 193-212, https://doi.org/10.1179/174328007X160308
[17] J.-F. Xu, F. Liu, S.-J. Song, K. Zhang: Journal of Non-Crystalline Solids, Vol. 356, 2010, p. 1236-1245, https://doi.org/10.1016/j.jnoncrysol.2014.04.034
[18] M. Starink: Journal of Materials Science, Vol. 36, No. 18, 2001, p. 4433-4441, https://doi.org/10.1023/A:1017974517877
[19] G. Lothongkum, S. Ratanamahasakul, P. Wangyao: Acta Metallurgica Slovaca, Vol. 11, No. 1, 2005, p. 54-61
[20] W. Smith, J. Hashemi: *Fundamentos de la ciencia e ingeniería de materiales*, fifth ed., Mc-Graw Hill, Mexico, 2014

Acknowledgements

This work was partially supported by IFISUR-CONICET, by Laboratorio de Metalurgia y Tecnología Mecánica del Departamento de Ingeniería (UNS) and Comisión de Investigaciones Científicas de la Provincia de Buenos Aires (CICPBA). In addition, the authors wish to acknowledge to Universidad Pontificia Bolivariana.

FABRICATION OF TRANSPARENT $MgAl_2O_4$ SPINEL CERAMICS BY PECS PROCESSING OF COMBUSTION - SYTHESIZED NANOPOWDERS

Yen Ngoc Nguyen[1)], Tu Anh Dao[1)], Hai Minh Le[1)], Khanh Quoc Dang[1)2),] Makoto Nanko[3)]*
[1)] School of Materials Science and Engineering, Hanoi University of Science and Technology, Hanoi, Vietnam
[2)] Center for Rubber Science and Technology, Hanoi University of Science and Technology, Hanoi, Vietnam
[3)] Department of Mechanical Engineering, Nagaoka University of Technology, Nagaoka, Niigata, Japan

Received: 17.05.2019
Accepted: 08.08.2019

[*]Corresponding author: e-mail: khanh.dangquoc@hust.edu.vn, Tel.: +84 24 3868 0355, School of Materials Science and Engineering, Hanoi University of Science and Technology, No.1, Dai Co Viet Street, Hai Ba Trung, Hanoi, Vietnam

Abstract
Transparent $MgAl_2O_4$ ceramic could be found in a wide range of applications for both military and civil sector due to its high melting point, good mechanical properties, small refractive index (1.71) and its ability to allow light in range from UV to mid-IR to pass through. In the present work, transparent $MgAl_2O_4$ spinel ceramics were fabricated from metal nitrates via two steps. Firstly, the $MgAl_2O_4$ nanopowder was synthesized via solution combustion synthesis from the metal nitrates. Secondly, the powder was then consolidated by Pulsed Electric Current Sintering (PECS) technique to fabricate transparent ceramic. XRD patterns of the obtained powder showed the peaks of only $MgAl_2O_4$ phase. Besides, the atomic compositions of magnesium, aluminium and oxygen determined by EDX analysis were approximately corresponded to 1:2:4 of the molecular formula of $MgAl_2O_4$. After deagglomerating for 48 hours using soft ball-milling, the powder had the average particle of 27 nm. Transparent $MgAl_2O_4$ samples, which were sintered with two-step sintering mode of 1050^{o}C/60 minutes-1400^{o}C/20 minutes, permitted the transmission of visible and infrared light with the transmittance up to 80%, Vickers hardness of 14.2 GPa, and fracture toughness of 1.1 MPa.m$^{1/2}$. The results are a critical step toward fabrication of high-quality transparent ceramics from metal nitrates.

Keywords: $MgAl_2O_4$, transparent ceramic, combustion synthesis, PECS, two-step sintering

1 Introduction

Magnesium Aluminate ($MgAl_2O_4$) spinel is one of the most outstanding transparent ceramics due to its unique optical and mechanical properties, even at high temperatures [1,2]. Furthermore, such material can allow light to pass through in a wide range from ultraviolet to mid-infrared wavelength (0.2 - 6 μm) [1]. Transparent $MgAl_2O_4$ spinel ceramics have a variety of application such as solid-state lasers, scintillators, armours, optical devices, electro-optical devices, biomaterials etc. [1, 2].

Powder fabrication and sintering play a vital role in transparency of final $MgAl_2O_4$ products since they are directly responsible for the density and the purity of materials. For powder fabrication, chemical synthesis methods have been recently considered as an effective approach

DOI 10.12776/ams.v25i3.1313 p-ISSN 1335-1532
e-ISSN 1338-1156

to prepare powders with high purity and nanoscale particles. Among chemical synthesis methods, solution combustion synthesis has been received an increasing attention due to low temperature requirement, homogeneous products, and low-cost precursors [3]. Various recent studies have reported that solution combustion synthesis have been effective for preparation of ultrafine $MgAl_2O_4$ powders [4, 5]. However, deagglomeration was often required to isolate the nanoparticles.

Recently, PECS has emerged as an efficient method to produce transparent ceramics [6-9], especially transparent $MgAl_2O_4$ [10, 11]. This method can assist in increasing bulk density and reducing grain size in $MgAl_2O_4$ ceramics, which improve both the mechanical properties and the transparency of the materials. Morita et al. [12] successfully demonstrated the densification of a fine-grained transparent spinel only for a 20 minutes holding time at a low temperature of 1300°C with a pressure of 80 MPa by employing a low heating rate ≤ 10°C/min. It is proposed that a slow heating rate can satisfy high density and fine grain size at a low sintering temperature; however, it takes a prolonged time for sintering process. To overcome the issues, two-step sintering technique was applied because this method not only prohibits grain growth but also shortens sintering duration [13]. In this method, the first stage is performed at a relatively low temperature and is followed by a higher temperature stage. Feasibility of two-step sintering method has been reported [14, 15], however, there are few reports on the combination of two-step sintering and PECS [16, 17, 18].

In this work, the feasibility of transparent $MgAl_2O_4$ ceramics fabrication from metal nitrates via solution combustion synthesis and two-step PECS sintering was investigated.

2 Experimental procedure

The starting materials were $Al(NO_3)_3.9H_2O$ and $Mg(NO_3)_2.6H_2O$ as oxidizers, and an urea (CH_4N_2O) as fuel. These materials have purity of 99% and were purchased from Xilong Scientific Co. Ltd., China. Precursor mixture was stoichiometrically balanced by a molar ratio of 3:6:20, and then dissolved in distilled water. Subsequently, the solution was placed in an electric resistance furnace (Linn HT1300, Germany) and it was heated at 500°C. The combustion reaction occurred according to the following reaction [2] to form a voluminous product.

$$3Mg(NO_3)_2\,(aq) + 6Al(NO_3)_3\,(aq) + 20CH_4N_2O\,(aq) \rightarrow 3MgAl_2O_4(s) + 20CO_2(g) + 40H_2O(g) + 32N_2(g) \quad (1.)$$

The synthesized product was deagglomerated for 48 hours in a highly pure ethanol solution using alumina balls with ball-powder mass ratios of 20/1. The milled powder was dried at 120°C for 24 hours and then calcined at 1100°C for 2 hours. As-received powders were fine but not showed spherical shape like other alloys [19]. The obtained powder was sintered by PECS machine (LABOX 1550i75S, Japan) in a graphite die with diameter of 10 mm, with a heating rate of 100°C/min and a uniaxial pressure of 100 MPa. Two-step sintering profile was applied with first-step temperature of 1050°C for 60 minutes and second-step temperature of 1400°C for 20 minutes. After sintering, samples were ground and polished by a slurry of Al_2O_3 powder with particle size of 0.05 μm for 80 hours.

The phase analysis was carried out by X-ray diffraction (Siemens D5000, Germany) using Cu Kα radiation. Morphology was characterized by a field-emitting scanning electron microscope (Hitachi S4800, Japan). The particle size and the size distribution were determined by ImageJ software through SEM images. Energy dispersive analysis (EDX) was performed to identify the elements that present in synthesized powders. Transmission spectrum was investigated by

DOI 10.12776/ams.v25i3.1313 p-ISSN 1335-1532
e-ISSN 1338-1156

ultraviolet-visible (UV-Vis) spectrophotometer (Shimadzu UV-1800, Japan) and Fourier-transform infrared (FTIR) spectrophotometer (Jasco FT/IR 4600, Japan). The Vickers hardness was tested by micro hardness tester (Struers Duramin 2, Germany).

3 Results and discussion

XRD patterns of combustion-synthesized product before and after annealing at 1100°C in air for 2 hours are shown in **Fig. 1**. The pattern of combustion-synthesized product before annealing shows 4 peaks at 2θ of 36.81°, 44.79°, 59.38°, 65.24° corresponding to magnesium aluminate spinel phase as given in the ICDD 01-082-2424 file. The broaden peaks reveal a poor crystallinity of combustion-synthesized product. After annealing, almost all the main $MgAl_2O_4$ reflections appeared in the XRD pattern are detected at 2θ of 31.29°, 36.81°, 38.52°, 44.79°, 56.21°, 59.38° and 65.24°. The peaks of $MgAl_2O_4$ phase are more intensive and well-defined indicating a good crystallinity of the annealed product. In addition, no peaks of impurities observed implies that the combustion synthesis process was operated in a well-controlled condition.

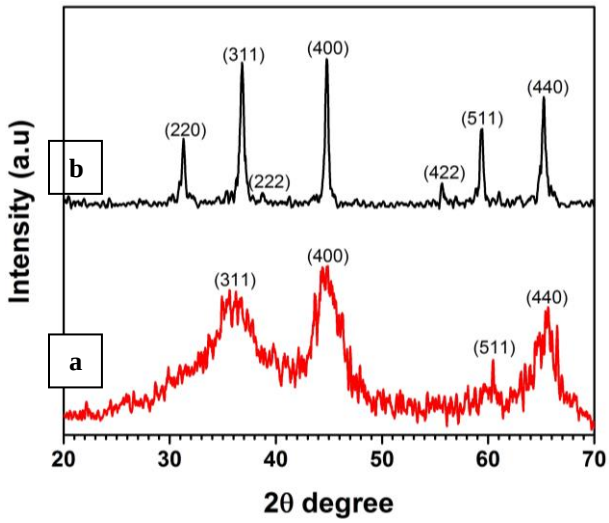

Fig. 1 XRD patterns of combustion-synthesized products before (a) and after (b) annealing at 1100°C in air for 2 hours

The morphology of the combustion-synthesized $MgAl_2O_4$ product characterized by SEM observation appeared in the form of large agglomerates of fine spherical particles (**Fig. 2a,b)**. The average sizes of particles and agglomerates are 20 nm and 8 μm, respectively. EDX pattern (**Fig. 2c**) acquired at the agglomerates shows that magnesium, aluminium and oxygen were the only detected elements with an atomic ratio of approximately 1:2:4. It is concluded that combustion-synthesized product possesses a relative high purity.

Soft-ball-milling is often required to isolate the $MgAl_2O_4$ particles. **Fig. 3a** shows SEM image of the $MgAl_2O_4$ powders milled for 48 hours with ball-powder mass ratio of 20/1. The milling process has a great influence on deagglomeration of particles. After milling, the amount of particle agglomerates significantly decreases. The agglomerate-size distribution and the percentage of particle volume of the $MgAl_2O_4$ powders milled is presented in **Fig. 3b**. The

DOI 10.12776/ams.v25i3.1313 p-ISSN 1335-1532
e-ISSN 1338-1156

milling process reduced the agglomerate proportional volume; hence the size distribution becomes uniform. The average agglomerate size is approximately 27 nm.

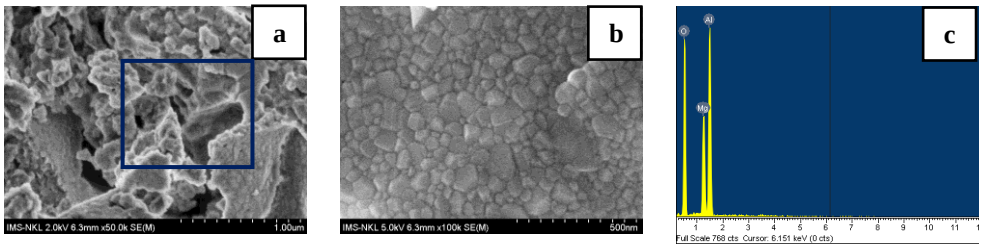

Fig. 2 SEM images of $MgAl_2O_4$ product before annealing at different magnifications of (a) 50kX and (b) 100kX and (c) corresponding EDX spectrum

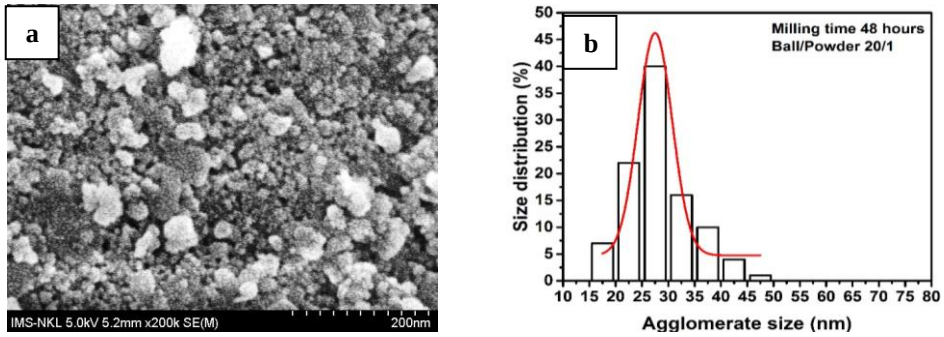

Fig. 3 SEM image (a) and agglomerate-size distribution (b) of $MgAl_2O_4$ powder milled for 48 hours with ball-powder ratio of 20/1

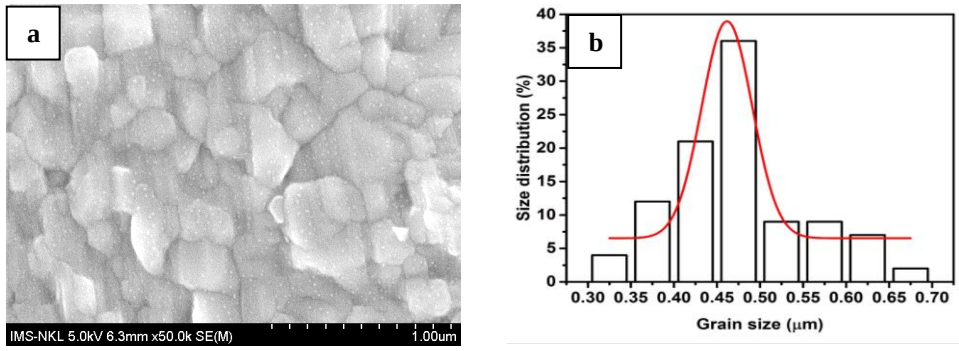

Fig. 4 SEM image (a) and grain size distribution (b) of $MgAl_2O_4$ sample sintered via two - step sintering mode of 1050ºC/60 minutes - 1400ºC/20 minutes

PECS process was carried out on the obtained nanopowders via two-step sintering mode of 1050ºC/60 minutes-1400ºC/20 minutes. Morphology of the sintered $MgAl_2O_4$ sample showed no residual pores on the thermal-etched polished surface (**Fig. 4a)**. Moreover, most of the grains were in submicron sized and the interparticle necks were not occurred in comparison with sintered alloys [20]. Grain sizes distribute in a narrow range from 0.3 μm to 0.7 μm with the average value of 0.48 μm (**Fig. 4b)**.

DOI 10.12776/ams.v25i3.1313 p-ISSN 1335-1532
e-ISSN 1338-1156

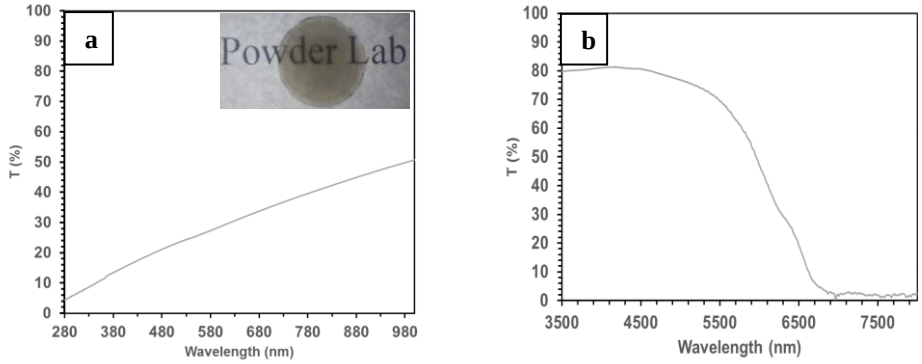

Fig. 5 Transmission spectrum of transparent $MgAl_2O_4$ ceramic samples in (a) ultraviolet-visible range (280-1000 nm) and (b) infrared range (3500-8000 nm)

The appearance of $MgAl_2O_4$ samples produced by PECS via sintering mode of 1050ºC/60 minutes-1400ºC/20 minutes (inset of **Fig. 5a)** showed a good transparency by naked eyes. **Fig. 5** represents transmission spectrum of $MgAl_2O_4$ samples in ultraviolet-visible range (wavelength, λ = 280-1000 nm) and infrared range (3500-8000 nm) with the thickness converted into 1 mm. The samples have poor transmittances in ultraviolet range. At visible wavelength, the transmittance values linearly increase, and reach the maximum value up to 80% in infrared range, which is close to the theoretical maximum of transmission (87%) [3]. Additionally, the transmittance begins to drop dramatically at 5500 nm and decreases to 0% at 7000 nm. The transmission evaluated at wavelengths of 700 nm (T_{700}) and 4000 nm (T_{4000}) are about 40% and 80%, respectively. The values of the Vickers hardness with a load of 20N and the fracture toughness K_{IC} calculated by using impression diagonals from Vickers hardness tips [21] of $MgAl_2O_4$ samples are 14.2 GPa and 1.1 MPa.m$^{1/2}$, respectively.

In general, transparent $MgAl_2O_4$ ceramics have been successfully fabricated from metal nitrates by the combination of two processes: solution combustion synthesis and spark plasma sintering via two-step temperature profile. The results obtained by this method are favourable compared with the previous results obtained for single-step-SPS processing. For a 20 nm co-precipitated powder, which is quite similar to the one in the present study, transparent $MgAl_2O_4$ spinel ceramics were achieved by single-step-SPS processing at 1550ºC for 3 minutes under an applied pressure of 50 MPa and a heating rate of 100ºC/min [22]. Transmittances of sintered samples are about 46% at 550 nm and 83% in the infrared range. Benaissa et al. proposed that sintering temperature can be reduced by using a low heating rate [23]. The commercial high purity powder with an average particle size of 50 nm (S30R, France) was single-step-SPS-sintered at 1300ºC under a pressure of 73 MPa with various steps of heating rate, i.e. 100ºC/min to 800ºC then 10ºC/min up to 1100ºC and 1ºC/min up to the final temperature. The transmission reached 70% at λ=550 nm and 78% at λ=1100 nm. The Vickers hardness and fracture toughness reached 18 GPa and 2.2 MPa.m$^{1/2}$, respectively. Their results presented a higher transmittance than in the present case. It might be caused by purity or agglomerate size distribution of the combustion synthesized powders. The control of $MgAl_2O_4$ nanopowders characteristics could be obtained by optimizing the elaboration conditions.

4 Conclusions

Transparent $MgAl_2O_4$ were successfully fabricated from metal nitrates via two-step process including solution combustion synthesis and PECS processing. The product obtained from

DOI 10.12776/ams.v25i3.1313 p-ISSN 1335-1532
e-ISSN 1338-1156

combustion reactions existed only single phase of $MgAl_2O_4$ and presented. Microstructure was in the form of large agglomerates of the fine spherical particles. After milled for 48 hours with ball-powder ratio of 20/1, $MgAl_2O_4$ powder had homogeneous distribution with a nanoscale average size (27 nm). Transparent $MgAl_2O_4$ ceramics was sintered via two-step sintering mode of 1050ºC/60 min-1400ºC/20 min using the combustion-synthesized nanopowders. Their microstructure showed submicron grain size (480 nm) with narrow size distribution. The optical transmittance of sintered $MgAl_2O_4$ ceramics was up to 40% at visible range and 80% at infrared range. Furthermore, sintered samples exhibited good mechanical properties, i.e. the Vickers micro-hardness of 14.2 GPa and the fracture toughness of 1.1 $MPa.m^{1/2}$.

References

[1] M. Rubat du Merac, H. J. Kleebe, M. M. Müller, I. E. Reimanis: Journal of the American Ceramic Society, Vol. 96, 2013, No. 11, p. 3341-3365, https://doi.org/10.1111/jace.12637
[2] I. Ganesh: International Materials Reviews, Vol. 58, 2013, No. 2, p. 63-112, https://doi.org/10.1179/1743280412Y.0000000001
[3] K. C. Patil: *Chemistry of Nanocrystalline Oxide Materials: Combustion Synthesis, Properties and Applications*, first ed., World Scientific, Singapore, 2008
[4] R. Ianoș, I. Lazau, C. Păcurariu, P. Barvinschi: Materials Research Bulletin, Vol. 43, 2008, No. 12, p. 3408-3415, https://doi.org/10.1016/j.materresbull.2008.02.003
[5] A. Choudhary, K. Rajeswari, Y. S. Rao, R. Johnson: Transactions of the Indian Ceramic Society, Vol. 73, 2014, p. 303-306, https://doi.org/10.1080/0371750X.2014.943911
[6] K. Q. Dang, M. Nanko, M. Kawahara, S. Takei: Materials Science Forum, Vol. 620-622, 2009, p. 101-104, https://doi.org/10.4028/www.scientific.net/MSF.620-622.101
[7] K. Q. Dang, M. Nanko: IOP conference series Materials Science and Engineering, Vol. 20, 2011, 012004, p. 1-7, https://doi.org/10.1088/1757-899X/20/1/012004
[8] K. Q. Dang, S. Takei, M. Kawahara, M. Nanko: Ceramics International, Vol. 37, 2011, No. 3, p. 957-963, https://doi.org/10.1016/j.ceramint.2010.11.009
[9] H. H. Nguyen, M. Nanko, K. Q. Dang: Journal of the Ceramic Society of Japan, Vol. 124, 2016, No. 4, p. 354-359, https://doi.org/10.2109/jcersj2.15258
[10] G. Bonnefont, G. Fantozzi, S. Trombert, L. Bonneau: Ceramics International, Vol. 38, 2012, No. 1, p. 131-140, https://doi.org/10.1016/j.ceramint.2011.06.045
[11] C. Wang, Z. Zhao: Scripta Materialia, Vol. 61, 2009, No. 2, p. 193-196, https://doi.org/10.1016/j.scriptamat.2009.03.039
[12] K. Morita, B. N. Kim, K. Hiraga, H. Yoshida: Scripta Materialia, Vol. 58, 2008, No. 12, p. 1114-1117, https://doi.org/10.1016/j.scriptamat.2008.02.008
[13] M. Y. Chu, L. C. Jonghe, M. K. Lin, F. J. Lin: Journal of the American Ceramic Society, Vol. 74, 1991, No. 11, p. 2902-2911, https://doi.org/10.1111/j.1151-2916.1991.tb06861.x
[14] F. J. Lin, L. C. Jonghe, M. N. Rahaman: Journal of the American Ceramic Society, Vol. 80, 1997, No. 9, p. 2269-2277, https://doi.org/10.1111/j.1151-2916.1997.tb03117.x
[15] I. W. Chen, X. H. Wang: Nature, Vol. 404, 2000, p. 168-171, https://doi.org/10.1038/35004548
[16] L. An, A. Ito, T. Goto: Journal of the European Ceramic Society, Vol. 31, 2011, No. 9, p. 1597-1602, https://doi.org/10.1016/j.jeurceramsoc.2011.03.014
[17] M. Nanko, K. Q. Dang: Advances in Applied Ceramíc, Vol. 113, 2014, No. 2, p. 80-84, https://doi.org/10.1179/1743676113Y.0000000109

DOI 10.12776/ams.v25i3.1313 p-ISSN 1335-1532
e-ISSN 1338-1156

[18] M. Nanko, K. Q. Dang: Pulsed Electric Current Sintering of Transparent Alumina Ceramics, In: *Sintering Techniques of Materials*, Edited by A. Lakshmanan, InTech, Croatia, 2015, p. 3-24, http://dx.doi.org/10.5772/59170
[19] D. Manfredi, R. Bidulský: Acta Metallurgica Slovaca, Vol. 23, 2017, No. 3, p. 276-282, http://dx.doi.org/10.12776/ams.v23i3.988
[20] R. Bidulsky et al.: Acta Physica Polonica A, Vol. 128, 2015, No. 4, p. 647-650, http://dx.doi.org/10.12693/APhysPolA.128.647
[21] A. G. Evans, E. A. Charles: Journal of the American Ceramic Society, Vol. 59, 1976, No. 7-8, p. 371-372, https://doi.org/10.1111/j.1151-2916.1976.tb10991.x
[22] M. Suarez, V. Rocha, A. Fernandez, J. L. Menendez, R. Torrecillas: Ceramics International, Vol. 40, 2014, p. 4065-4069, https://doi.org/10.1016/j.ceramint.2013.08.060
[23] S. Benaissa, M. Hamidouche, M. Kolli, G. Bonnefont, G. Fantozzi: Ceramics International, Vol. 42, 2016, No. 7, p. 8839-8846, https://doi.org/10.1016/j.ceramint.2016.02.130

Acknowledgements
This research is funded by Vietnam Ministry of Education and Training under project number B2018-BKA-63.

INFLUENCE OF GATE SHAPE AND DIRECTION DURING CENTRIFUGAL CASTING ON ARTIFICIAL LUMBAR DISC MODEL OF Cp-Ti

Lilik Dwi Setyana[1)], Muslim Mahardika[1,2)], Sutiyoko[3)], Suyitno[1,2)]*
[1)] Department of Mechanical and Industrial Engineering, Faculty of Engineering, Universitas Gadjah Mada Yogyakarta, 55281, Indonesia
[2)] Center for Innovations of Medical Devices, Universitas Gadjah Mada Yogyakarta, 55281, Indonesia
[3)] Foundry Department, Manufacturing Polytechnic of Ceper, Klaten, Indonesia

Received: 26.07.2019
Accepted: 06.09.2019

[*]Corresponding author: Email: lilikdwi_s@ugm.ac.id, Tel.:08562856934, Department of Mechanical and Industrial Engineering, Faculty of Engineering, Universitas Gadjah Mada Yogyakarta, 55281, Indonesia

Abstract
Shape and direction of gate in centrifugal casting affected the microstructures and defects in castings. The purpose of this research was to determine the effects of gate shape and direction in centrifugal casting toward on porosity, density, roughness, and microstructures on the artificial lumbar disc model. The main shapes of the gate were circular and rectangular cross-section. The circular cross-section gate shape was used for two different directions of artificial lumbar discs; vertical, and horizontal. Furthermore, the rectangular cross-section gate shape consisted of three different directions; oblique clockwise, oblique counter-clockwise and perpendicular towards the mold. The rotational mold was conducted at a speed of 60 rpm. The results showed that the rectangular cross-section gate shape with the oblique direction same with the rotation of the mold produced artificial lumbar disc model that had the smallest porosity area among the other directions. It was the best shape and direction of the gate among the others which had the smallest porosity area (0.68%), highest density (4.517 g/cm^3), and smoothest roughness (8.76 μm). In the sub-surface, the microstructure of α-case was formed. The thickness and hardness of the α-case in this design were 50-100 μm and 760 VHN, respectively. Hence, the rectangular cross-section gate shape with the oblique direction same with the rotation of the mold was appropriate to be applied in the manufacture of an artificial lumbar disc model.

Keywords: Gating system, Foundry, Centrifugal casting, Artificial lumbar disc model

1 Introduction

Centrifugal casting has several advantages such as accurate dimensions, smooth surface finish, limited gas porosity, faster solidification, and effective cost rather than the traditional gravity casting method [1, 2]. These advantages are caused by the distribution of the liquid metal into the mold which is using forces generated from the centripetal acceleration of a rotating mold. The centrifugal force is a function of radius, metal density, and rotational speed [1]. The rotational speed that directly controls the pressure distribution affects the shrinkage cavity. In general, increasing centrifugal force can decrease defects [3].

The gating system is an essential element in the casting process, which affects the molten metal flow behavior [4]. The purpose of gating system design in centrifugal casting is to get the product

DOI 10.12776/ams.v25i3.1315 p-ISSN 1335-1532
e-ISSN 1338-1156

with minimal defects such as porosity. Porosity can occur due to the trapped gas or shrinkage during the cooling process [5-7]. Shrinkage control is carried out to produce defect-free products [8]. Modifications and trial errors of gating system design are less efficient and high cost to acquire good quality products. Therefore, computer simulation is sufficient to be used to plan the gating system design. The simulation results show the suitability with experimental data such as liquid solidification, porosity area, trapped gas, and filling behavior occurred in the foundry process [6, 9-11].

The direction, position, and cross-section of gating system design on centrifugal casting are made to get products with minimal shrinkage porosity. Gate shapes that often used are circular [4], rectangular [10, 12-14], and hexagonal [10] cross-section with perpendicular direction to the mold. The circular cross-section of the gate shape has a higher molten metal filling speed rather than the rectangular or hexagonal [10]. Viscosity increases rapidly in rectangular and hexagonal cross-section which has a closer gate wall distance to the cross-section center than a circular one. This condition affects porosity, which tends to be more numerous [10].

The internal porosity can be reduced by adjusting a high rotational speed (≥180 rpm) [15]. On the other hand, it can reduce the mechanical properties of the product. In the gating system, decreasing cross-sectional area towards the mold cavity increased the pressure that will affect the tensile strength [16]. On the contrary, increasing cross-sectional area towards the mold cavity reduced turbulence [16]. Research of gate shape and direction on centrifugal casting is still needed to make the best design so that liquid metal can enter the mold cavity with higher pressure and low turbulence. Changing geometry, shape, and number of the gate can be the solution affected higher pressure and low turbulence [13]. On the other hand, researches on the oblique direction of gating system design are still unavailable.

However, the final products of centrifugal casting still have porosity even though circular, rectangular, or hexagonal cross-sections of gate were used. Gate design with the oblique of clockwise or counter-clockwise directions, which purposed to increase the speed of molten metal in entering the mold, has not been applied. The study was conducted to determine the effects of shape, direction, and position of gate design toward on porosity, density, microstructure, hardness, and surface roughness of the artificial lumbar disc model. Artificial lumbar disc model in this research is prepared for the spinal implant. Porosity, density, and hardness controls of the product must be carried out so that the product strength is adequate. The surface roughness of the product must be adjusted with the bioactive area [17].

2 Material and Methods

2.1 Used Material and Mold

This study used commercial pure titanium (Cp-Ti) with 99.72 wt% Ti; 0.17 wt% Fe; and 0.11 wt% gaseous element. Analysis of composition used EDS (Quanta x50 SEM Series). Cp-Ti was melted at a temperature of 1700^{o}C, then poured in an artificial lumbar disc model shell mold. The shell mold was made from the zirconium-based ceramic material consisted of 8 layers. The filling time of the centrifugal casting when pouring was constant with the molten metal pouring rate of about 0.12 kg/s. Furthermore, the mold was rotated at 60 rpm when molten metal was poured. The above processes were carried out in the vacuum furnace (Flash caster, Japan).

The schematic product geometry and product of artificial lumbar disc model can be seen in **Fig.1**. The outer diameter of the product was 30 mm, then the radius of the ball-on-socket was 13 mm with 2 mm of depth.

DOI 10.12776/ams.v25i3.1315 p-ISSN 1335-1532
e-ISSN 1338-1156

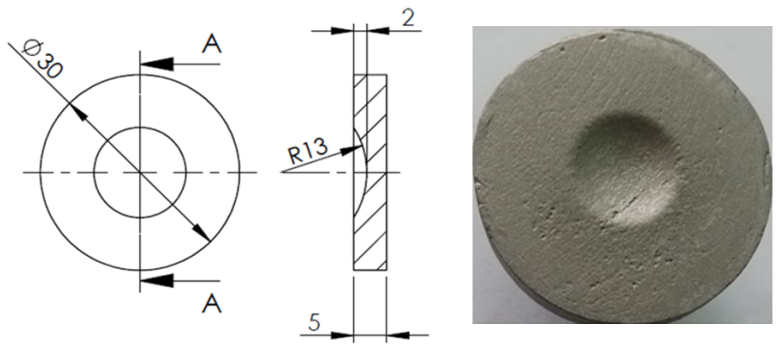

a. b.

Fig. 1 The schematic geometry of product (a) and product (b) of artificial lumbar disc model

2.2 Gate Shape and Direction

The shape and geometry of gate can be seen in **Fig.2**. The main shapes of gate design were circular (**Fig. 2.a**) and rectangular cross-section (**Fig. 2.b**). The geometry of gate cross-section area decreased gradually to increase the pressure of molten metal when entering the mold. The length of each gate types was 15.0 mm. The circular cross-section area was 78.5 mm^2 then decreased gradually until 19.6 mm^2 when entering the mold. While the rectangular cross-section area was 70.0 mm^2 then decreased gradually until 30 mm^2 when entering the mold.

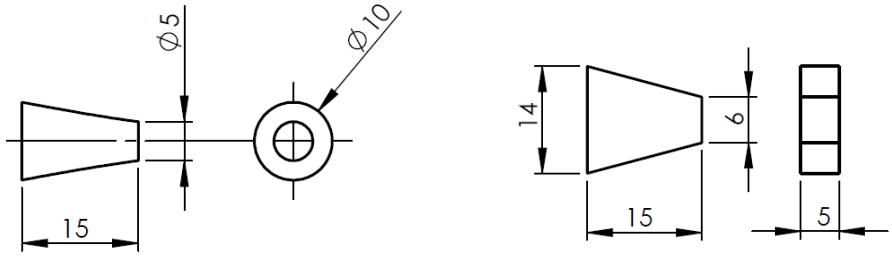

a. b.

Fig. 2 The gates shape and geometry

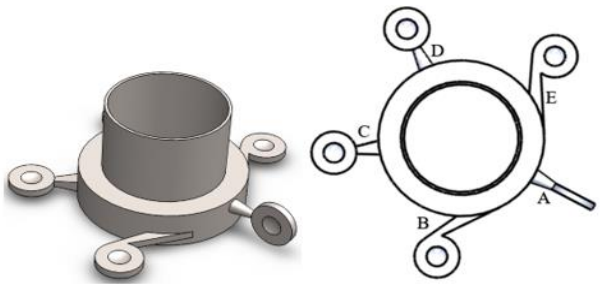

Fig. 3 The gates position and direction of artificial lumbar disc model

The gate position and direction was shown in **Fig. 3**. The circular cross-section design was used for two different directions of artificial lumbar discs, namely vertical “A” and horizontal “D”. The

DOI 10.12776/ams.v25i3.1315 p-ISSN 1335-1532
e-ISSN 1338-1156

direction of this design was perpendicular toward the mold. The rectangular cross-section design consisted of three different directions, namely oblique clockwise "B", perpendicular "C", and oblique counter-clockwise "E" toward the mold. All positions of the mold on the rectangular gate design were horizontal. The oblique direction of the clockwise and counter-clockwise was 45^{o} toward the mold.

The Gate shape and direction of artificial lumbar disc model was simulated using Solid Cast 7.0.2 software to predict the porosity occurred. The parameters used in the simulation refer to the research that has been done before [5, 18].

2.3 Observations and Tests

The observations carried out in this research included porosity, and microstructures. The porosity phenomena were analyzed using dye penetrant and a stereo zoom microscope (SZ-PT, Olympus, Japan). Porosity calculations that used visual inspection with millimeter blocks were carried out by comparing the area of porosity with the total area of the product. The number of pores was determined by counting manually. The microstructure characterization was analyzed using a metallurgical microscope (PME 3, Olympus, Japan) and SEM (Quanta x50 SEM Series). Preparation was done with #180 to #8000 sandpapers to obtain a smooth surface, then metal was polished. While to uncover the microstructure (etching process), a Kroll reagent was used.

The tests carried out in this research included hardness, surface roughness, and density. The hardness was obtained from the outer of the sub-surface to the inner of a cross section spanning sample using a microhardness tester (HMV-M3, Shimadzu, Japan). The distance among each test points of hardness test was 50 μm with a load of 2 N, then hold for 5 s. Surface roughness (Ra) testing was carried out in five places in the upper surface of each product using a profilometer (Surfcorder SE 1700, Fowler). The Ra tester was calibrated on the standard specimen (Ra being 3.0 μm). The density calculation was done by dividing the weight with the volume of product. The weight was measured by using analytical balancing (Sartorius AG Gottingen LC 12018, Germany)

3 Results

3.1 Porosity

The casting product was shown in **Fig. 4.a.** All gates design allow the molten metal flows properly so that there are no defects on the surface of the product. The simulation result using Solid Cast software (**Fig. 4.b**), shows there is porosity that can be seen through different colors. The product with the circular cross-section gate shape on the vertical direction (A) only has a few porosities. However, the horizontal direction (D) has the most porosities. While the rectangular cross-section gate design with oblique clockwise (B), and perpendicular (C) appear to have almost the same porosity, while oblique counter-clockwise (E) has the smallest porosity.

The porosity location of all products on the experiment results is spreading, as shown in **Fig. 5**. The porosity in all gate design is found in the middle area between the thickness of the products. Internal shrinkage porosity (**Fig. 5.F**) is found with irregular shapes in different sizes (50-200 μm). The internal shrinkage porosity that occurs has a crack tail. Crack tail (**Fig. 5.G**) occurs in transgranular (1) and intergranular (2) of grains.

The percentage of porosity area can be seen in **Table 1**. Product with the circular cross-section gate design on the vertical direction only has a few porosities (0.69%) compared to the total area

DOI 10.12776/ams.v25i3.1315 p-ISSN 1335-1532
e-ISSN 1338-1156

of the product. The porosity tends to congregate with a size of about 50-150 μm. However, the horizontal direction has the most porosities (1.29%). The porosity in this design tends to congregate with a size bigger than in vertical direction (about 50-200 μm).

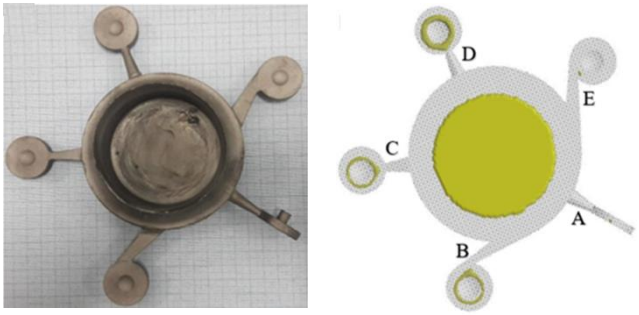

a. b.

Fig. 4 The casting product (a) and simulation result (b)

Table 1 The porosity area of various gate shape and direction

Type	Total Area	Porosity	Percentage
	(mm^2)	(mm^2)	(%)
A	10920	75	0,687
B	10920	254	2,326
C	10920	88	0,806
D	10920	141	1,291
E	10920	74	0,678

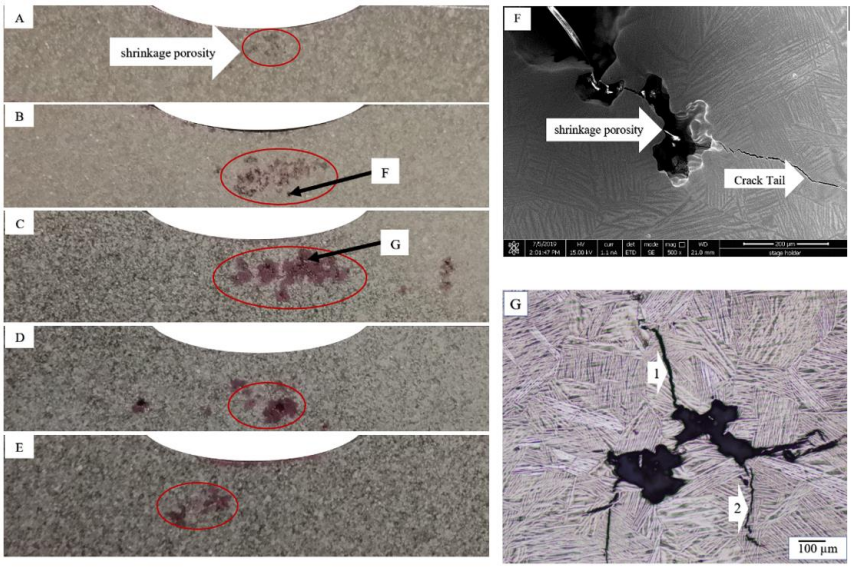

Fig. 5 The location of shrinkage porosity on product (A – E) with various types of gate shape and direction; and enlargements of shrinkage porosity (F and G in products B and C)

DOI 10.12776/ams.v25i3.1315 p-ISSN 1335-1532
e-ISSN 1338-1156

Furthermore, the rectangular cross-section gate design with oblique clockwise, perpendicular and oblique counter-clockwise have 2.33%, 0.81%, and 0.68% porosities area respectively compared to the total area of the product. The porosity on the rectangular cross-section with oblique clockwise spreads with a size of about 50-150 μm. While on the perpendicular and oblique counter-clockwise direction has a size of about 50-200 μm.

3.2 Density

The products density with various types of gate design is shown in **Fig. 6**. The density of product with the circular design for vertical direction is 4,515 g/cm^3. While product with a horizontal direction has a density of 4,511 g/cm^3. Furthermore, the density of product with the rectangular cross-section with oblique clockwise, oblique counter-clockwise and perpendicular towards the mold are 4,510 g/cm^3, 4,511 g/cm^3, and 4,517 g/cm^3 respectively.

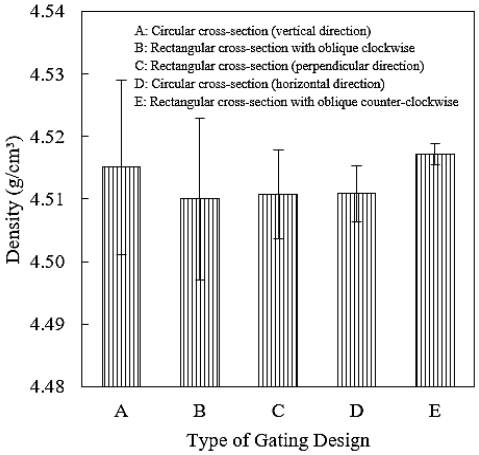

Fig. 6 The density of product with various types of gate shape and direction

3.3 Hardness and Microstructure

Fig. 7 shows the results of the hardness test. The product with a circular design for vertical and horizontal directions gate design have the same trend of hardness. The hardness with the circular design for vertical direction is 671 VHN on sub-surface, then drops significantly to 412 VHN at 250 μm from the surface. While product with a horizontal direction has a hardness of 732 VHN on sub-surface, then drops significantly to 362 VHN at 350 μm from the surface. Both products have relatively the same hardness (around 340 VHN) at a distance of 350 to 1.250 μm from the surface.

The types of α morphologies and equiaxed prior β grains were found in the microstructure of product in all kinds of gate design (**Fig. 8**). It is supported by the previous research result [19]. The types of α-morphologies are known as α-case (a), prior β grain boundaries (b), widmanstaten α (c) and fine acicular α (d) at different locations. The morphologies of grain are similar with the previous research [20]. The microstructure of the outer edge has lamellar shaped with a random, tight, and small arrangement.

In the sub-surface, the microstructure of α-case is formed. The thickness of α-case is about 50-100 μm and 250-300 μm with circular cross-section on vertical (**Fig. 8.A**) and horizontal (**Fig. 8.D**) direction respectively. The α-case on the horizontal direction has a crack (e) for about 150-300 μm length. While the rectangular cross-section with oblique clockwise (**Fig. 8.B**),

DOI 10.12776/ams.v25i3.1315 p-ISSN 1335-1532
e-ISSN 1338-1156

perpendicular to the mold (**Fig. 8.C**), and oblique counter-clockwise (**Fig. 8.E**) are 200-250 μm, 150-200 μm, and 50-100 μm respectively. The α-case on rectangular cross-section with oblique clockwise has a crack (e) for about 150-300 μm length.

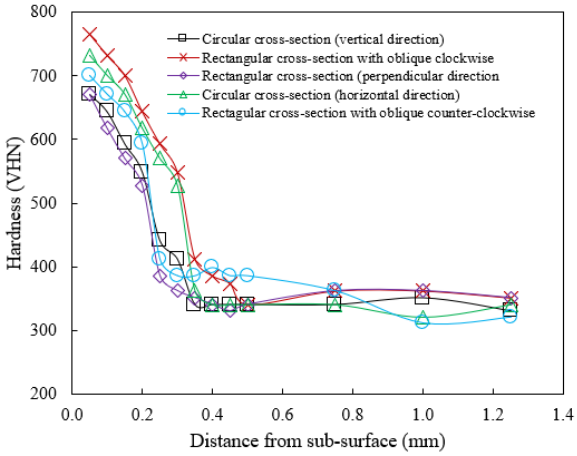

Fig. 7 The hardness of product with various types of gate shape and direction

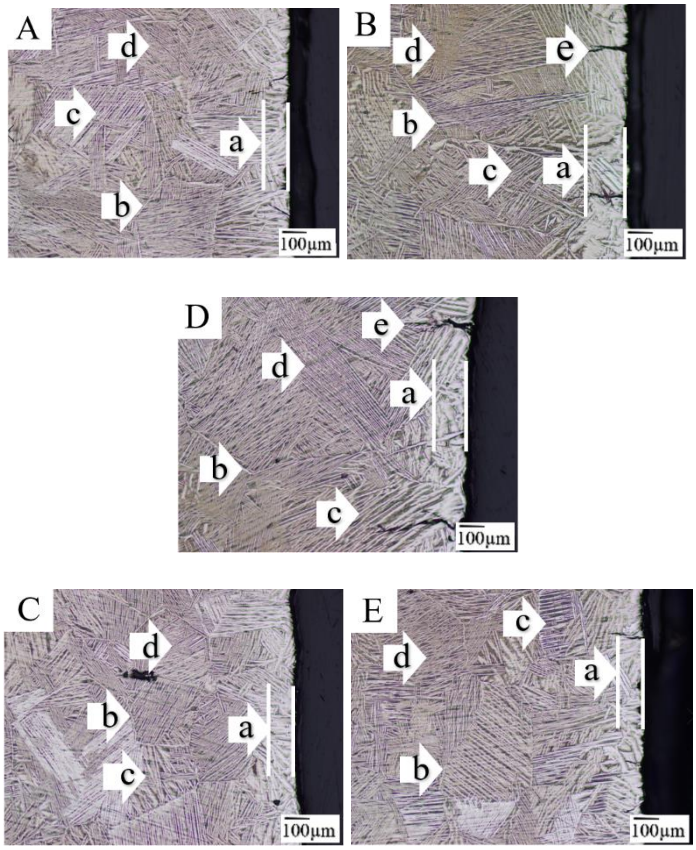

Fig. 8 The microstructures in the subsurface of the product

DOI 10.12776/ams.v25i3.1315
p-ISSN 1335-1532
e-ISSN 1338-1156

Furthermore, the hardness of the product with the rectangular cross-section with oblique clockwise, oblique counter-clockwise, and perpendicular towards the mold also have the same trend in reducing the hardness. The hardness of product with oblique clockwise drops from 766 VHN in the sub-surface until 412VHN at the 350 μm from the surface. Then oblique counter-clockwise at the hardness of 701 VHN drops until 412 VHN at the 250 μm. Lastly, the perpendicular towards the mold also drops significantly from 671 VHN to 386 VHN in the distance of 250 μm from the surface. All products have relatively the same hardness (around 340 VHN) at a distance of 350 to 1.250 μm from the surface.

3.4 Surface Roughness

The surface roughness (Ra) of products are ranged from 8.76 to 11.07 μm (**Fig. 9**). The Ra of the product with circular cross-section on vertical and horizontal direction are 8.94 μm and 10.57 μm. While the Ra of the product with the rectangular cross-section with oblique clockwise, oblique counter-clockwise and perpendicular towards the mold are 11.07 μm, 8.76 μm, and 9.36 μm respectively. The product with rectangular cross-sections with oblique counter-clockwise has the smoothest surface among the others.

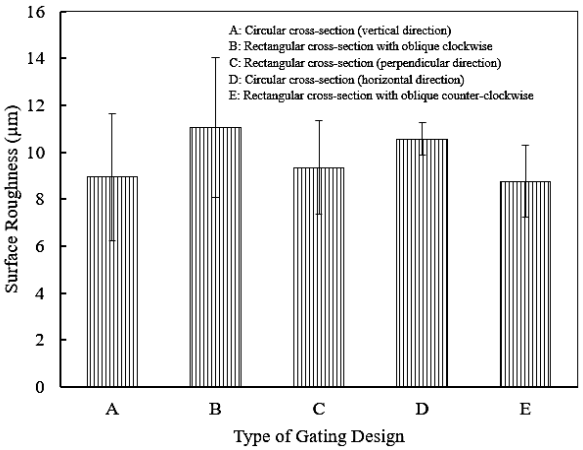

Fig. 9 The surface roughness of product with various types of gate shape and direction

4 Discussion

Product with the circular cross-section gate shape on the vertical direction has less porosities, higher density, and smoother surface than the horizontal one. This condition caused by the vertical direction has a smaller vortex space compared to the horizontal during the pouring process. The bigger diameter of the vortex flow runner in the casting product will directly proportional with the average flexural strength [4]. The porosities in both designs congregate with an irregular spherical shape with a crack tail (**Fig. 5.F**). The size of porosity in the vertical direction of the product is smaller than the horizontal one.

The vertical and horizontal direction of products has relatively the same trend of hardness. The α-case is formed on the sub-surface of the region. The α-case has a thickness of 50-300 μm with a hardness of 760 VHN. This is confirmed with the results of a study [21]. The α-case on the horizontal direction is thicker and harder than the vertical one. This condition happens because the vertical position that has a small vortex space may have a higher cooling rate compared to the

DOI 10.12776/ams.v25i3.1315 p-ISSN 1335-1532
e-ISSN 1338-1156

horizontal one during the solidification process. Higher cooling rate makes the α-case thinner that prevents oxygen diffusion to occur [22].

The rectangular cross-section gate shape with an oblique counter-clockwise direction has the smallest porosity area, highest density, and smoothest surface among other directions. The direction of this gate is aligned with the rotation of the mold. The molten metal becomes easier and faster to enter the mold cavity when pouring; then it freezes immediately. Losses friction between the molten metal and the gate wall become small. This design has the thinnest α-case (with no crack) among other directions.

Furthermore, the design with the oblique counter-direction of the rotation of the mold has the largest porosity area, lowest density, and roughest surface, among other directions. The molten metal is difficult to get in the mold cavity when the direction of gate is opposite toward the mold rotation. This condition happens because there are minor and major losses exist in the gate wall. These major losses are caused by friction along the molten metal flow against the gate wall, while minor losses are caused by sharp turns. Major and minor loses cause fluidity to decrease rapidly, so porosity will be easier to occur [10]. This design has the thickest α-case among other directions, so there is crack. The α-case layer is hard and brittle with a high-stress concentration [21], so cracking happens easily.

The microstructure formed tends to be similar, which consists of some α morphologies types and equiaxed prior β grains. The different morphologies nucleate, including the α grain boundary, make prior β grains remain observable. The microstructure on the subsurface is transformed from fine grain to slightly become coarse one in the inner area. This transformation of grain is similar with the previous research [3].

5 Conclusion

The conclusions of this research are:

1. Product with the circular cross-section gate shape on the vertical direction has less porosities, higher density, and smoother surface than the horizontal one.
2. Product with the rectangular cross-section with the oblique counter-direction of the rotation of the mold has the largest porosity area, lowest density, and roughest surface among other directions.
3. The rectangular cross-section gate shape with oblique same with the mold rotation produces an artificial lumbar disc model with the smallest porosity area (0.68%), the highest density (4,517 g/cm^3), and the thinnest α-case (50-100 μm).
4. The rectangular cross-section gate shape with oblique direction same with the mold rotation can be applied to the manufacture of artificial lumbar disc model.

References

[1] W. S. Ebhota, A. S. Karun, F. L. Inambao: International Journal of Materials Research, Vol. 107, 2016, No. 10, p. 1-10, https://doi.org/10.3139/146.111423

[2] S. Wu, Q. Xu, X. Xue: Advanced Materials Research, Vol. 317-319, 2011, No. 456, p. 456-459, https://doi.org/10.4028/www.scientific.net/ AMR.317-319.456

[3] T. Prayoga, R. Dharmastiti, F. Akbar, Suyitno: Journal of Mechanical Science and Technology, Vol. 32, 2018, No. 1, p. 149-156, https://doi.org/10.1007/s12206-017-1216-8

[4] R. Ahmad, M.Y. Hasyim: Archives of Metallurgy and Materials, Vol. 56, 2011, No. 4, p. 991-997, https://doi.org/10.2478/v10172-011-0109-6

[5] Sutiyoko, Suyitno, M. Mahardika, A. Syamsudin: Archives of Foundry Engineering, Vol. 16, 2016, No. 4, p. 157-162, https://doi.org/ 10.1515/afe-2016-0102
[6] B. H. Hu, K. K. Tong, X. P. Niu, I. Pinwill: Journal of Materials Processing Technology, Vol. 105, 1999, No. 1-2, p. 128-133, https://doi.org/10.1016/S0924-0136(00)00546-X
[7] J. K. Kuo, P. H. Huang, H. Y. Lai, J. R. Chen, J. R: International Journal Advance Manufacture Technology. Vol. 92, 2017, No. 1-4, p. 1093-1103, https://doi.org/10.1007/s00170-017-0198-0
[8] S. Samavedam, S. Sundarrajan: Archives of Foundry Engineering, Vol. 16, 2016, No. 1, p. 61-68, https://doi.org/10.1515/afe-2016-0004
[9] B. D. Lee, U. H. Baek, J. W. Han: Journal of Materials Engineering and Performance, Vol. 16, 2011, No. 1, p. 1-9, https://doi.org/10.1007/ s11665-011-0111-1
[10] P. Suwankan, N. Sornsuwit, N. Poolthong: Key Engineering Materials, Vol. 659, 2015, p. 647-651, https://doi.org/10.4028/ www.scientific.net/KEM.659.647
[11] N. J. Humphreys, et al.: Applied Mathematical Modelling, Vol. 37, 2013, No. 14-15, p. 7633-7643, https://doi.org/10.1016/ j.apm.2013.03.030
[12] M. Gadalla, R. Habingreither, R. Cook: The Minerals, Metals and Materials Society, 2007, p. 39-45
[13] M. Masoumi, H. Hu, J. Hedjazi, M. A. Boutorabi: American Foundry Society, Vol. 05-152, 2005, No. 2, p. 1-12
[14] B. H. Hu, K. K. Tong, X. P. Niu, I. Pinwill: Journal of Materials Processing Technology, Vol. 105, 2000, p. 128-133, PII: S0924-0136(00)00546-X
[15] Y. Ling, J. Zhou, H. Nan, L. Zhu, Y. Yin: Journal of Materials Processing Technology, Vol. 251, 2018, p. 295-304, https://doi.org/10.1016/j.jmatprotec.2017.08.025
[16] O. Akinlabi, A. Ayodele: Acta Metallurgica Slovaca, Vol. 21, 2015, No. 2, p. 135-141, https://doi.org/10.12776/ams.v21li2.567
[17] P. J. Rao, M. H. Pelletier, W. R. Walsh, R. J. Mobbs: Orthopaedic Surgery, Vol. 6, 2014, p. 81–89, https://doi.org/10.1111/os.12098
[18] R. C. Atwood, P. D. Lee, R. V. Curtis, D. M. Maijer: Dental Material, Vol. 23, 2007, No. 1, p. 60-70, https://doi.org/10.1016/j.dental.2005.12.001
[19] K. M. Ibrahim, M. Mhaede, L. Wagner, L: Transactions of Nonferrous Metals Society of China, Vol. 21, 2011, No. 8, p. 1735-1740, https://doi.org/10.1016/S1003-6326(11)60923-0
[20] M. J. Bermingham, S. D. Donald, M. S. Dargusch, D. H. John: Journal Material Research, Vol. 23, 2008, No. 1, p. 97-104, https://doi.org/10.1557/JMR.2008.0002
[21] W. J. Boettinger, M. E. Williams, S. R. Coriell, U. R. Kattner, B. A. Mueller: Metallurgical and Materials Transactions B, Vol. 31, 2000, No. B, p. 1-9, https://doi.org/10.1007/s11663-000-0026
[22] D. Chan, V. Guillory, R. Blackman, K.H. Chung: The Journal of Prosthetic Dentistry, Vol. 78, 1997, No. 4, p. 400-404, https://doi.org/10.1016/S0022-3913(97)70048-9

Acknowledgement

The research was funded under dissertation grant by the Indonesian Ministry of Finance through Lembaga Pengelola Dana Pendidikan (LPDP). We thank the Department of Mechanical and Industrial Engineering Universitas Gadjah Mada for Observation and Testing equipment.